

PAPER • OPEN ACCESS

Flagellar length control in biflagellate eukaryotes: time-of-flight, shared pool, train traffic and cooperative phenomena

To cite this article: Swayamshree Patra *et al* 2020 *New J. Phys.* **22** 083009

View the [article online](#) for updates and enhancements.

You may also like

- [Physics of microswimmers—single particle motion and collective behavior: a review](#)
J Elgeti, R G Winkler and G Gompper
- [Transient pauses of the bacterial flagellar motor at low load](#)
A L Nord, F Pedaci and R M Berry
- [In-phase and anti-phase flagellar synchronization by waveform compliance and basal coupling](#)
Gary S Klindt, Christian Ruloff, Christian Wagner *et al.*

New Journal of Physics

The open access journal at the forefront of physics

Deutsche Physikalische Gesellschaft 

IOP Institute of Physics

Published in partnership
with: Deutsche Physikalische
Gesellschaft and the Institute
of Physics



PAPER

OPEN ACCESS

RECEIVED
6 March 2020

REVISED
28 May 2020

ACCEPTED FOR PUBLICATION
22 June 2020

PUBLISHED
5 August 2020

Original content from
this work may be used
under the terms of the
[Creative Commons
Attribution 4.0 licence](#).

Any further distribution
of this work must
maintain attribution to
the author(s) and the
title of the work, journal
citation and DOI.



Flagellar length control in biflagellate eukaryotes: time-of-flight, shared pool, train traffic and cooperative phenomena

Swayamshree Patra¹, Frank Jülicher²  and Debashish Chowdhury^{1,2} 

¹ Department of Physics, Indian Institute of Technology Kanpur, 208016, India

² Max-Planck Institute for the Physics of Complex Systems, Nöthnitzer Strasse 38, 01187 Dresden, Germany

E-mail: julicher@pks.mpg.de and debch@iitk.ac.in

Keywords: intraflagellar transport, flagellar length control, time-of-flight, totally asymmetric simple exclusion process, master equation

Abstract

Flagella of eukaryotic cells are transient long cylindrical protrusions. The proteins needed to form and maintain flagella are synthesized in the cell body and transported to the distal tips. What ‘rulers’ or ‘timers’ a specific type of cells use to strike a balance between the outward and inward transport of materials so as to maintain a particular length of its flagella in the steady state is one of the open questions in cellular self-organization. Even more curious is how the two flagella of biflagellates, like *Chlamydomonas reinhardtii*, communicate through their base to coordinate their lengths. In this paper we develop a stochastic model for flagellar length control based on a time-of-flight (ToF) mechanism. This ToF mechanism decides whether or not structural proteins are to be loaded onto an intraflagellar transport (IFT) train just before it begins its motorized journey from the base to the tip of the flagellum. Because of the ongoing turnover, the structural proteins released from the flagellar tip are transported back to the cell body also by IFT trains. We represent the traffic of IFT trains as a totally asymmetric simple exclusion process (TASEP). The ToF mechanism for each flagellum, together with the TASEP-based description of the IFT trains, combined with a scenario of sharing of a common pool of flagellar structural proteins in biflagellates, can account for all key features of experimentally known phenomena. These include ciliogenesis, resorption, deflagellation as well as regeneration after selective amputation of one of the two flagella. We also show that the experimental observations of Ishikawa and Marshall are consistent with the ToF mechanism of length control if the effects of the mutual exclusion of the IFT trains captured by the TASEP are taken into account. Moreover, we make new predictions on the flagellar length fluctuations and the role of the common pool.

1. Introduction

In a classic article, titled ‘on being the right size’, J B S Haldane [1] first analysed the physical reasons that explain why ‘for every type of animal there is a convenient size’. He focussed his analysis on the size of whole organisms. However, the mechanisms that ensure the ‘convenient’ size of a cell [2] and sub-cellular structures [3–5] have become a very active field of research in recent years. Membrane-bound organelles are prominent among the sub-cellular structures. Flagella of eukaryotic cells (not to be confused with bacterial flagella), which are the organelles of our interest in this paper, appear as long cell protrusions [6] (key features of its structure are summarized in the next section). The short eukaryotic flagella are often referred to as cilia. In this paper, we will use the terms ‘flagellum’ and ‘cilium’ interchangeably.

From the perspective of organelles size control, what makes flagella very interesting is not only the one-dimensional nature of the problem but also their highly dynamic lengths. The lengths of flagella change with time in sync with the cell cycle [7–9]. Even when their growth is complete, flagellar structure remains highly dynamic because each of the flagella continue to incorporate new proteins to make up for the high ongoing turnover, thereby maintaining a steady balance of the elongation and shortening [10, 11]. So,

the first challenging question is how a specific cell maintains this balance at a particular length of a flagellum.

The number of flagella vary from one species to another. Flagellar length control in biflagellated and multiflagellated cells are more interesting than that in monoflagellates. So, in the context of flagellar length control, the second challenging question is how biflagellated and multiflagellated cells coordinate the dynamics of their different flagella. For the sake of simplicity, in this paper, we consider only biflagellated eukaryotes for which the green algae *Chlamydomonas reinhardtii* (CR) serves as the most popular model organism [12, 13].

CR is an interesting organism for studying flagellar length control because CR can loose its flagella in three distinct ways: resorption, deflagellation and selective amputation. Even more interesting is the fact that the CR can successfully regenerate its flagella as well. Both the flagella of a CR are gradually retracted into the cell prior to the cell division [14]; this phenomenon is usually referred to as '*resorption*'. The flagellar components disassembled during resorption are returned to the cell body [9]. Flagellar disassembly [15] via resorption should be distinguished from '*deflagellation*' (also known as flagellar excision, flagellar shedding or flagellar autotomy) [16]. In the latter process, in response to wide varieties of stimuli, the axoneme is severed resulting in a complete loss of the flagellar components. Deflagellated CR cells can regenerate their flagella when stress causing stimulus disappears [17, 18]. One of the flagella, or a distal part of it, can be selectively amputated in controlled experiments. All the proteins constituting the severed part of the amputated flagellum are lost by the cell. The regeneration of the amputated flagellum and the concomitant *nonmonotonic* variation of the length of its unsevered partner display most vividly the cooperation of the dynamics of the two flagella. The model we develop here describes resorption, deflagellation as well as regeneration of flagella within a single theoretical framework.

Proteins are synthesized in the cell body, and not in the flagella. Therefore, the flagellar structural proteins are transported from the base to the tip of each flagellum by intraflagellar transport (IFT) [19–21]. Similarly, structural constituents of flagella that turn over are transported back to the cell body. IFT particles, which are multi-protein complexes at the core of the IFT machinery, operate essentially as the '*protein shuttles*' [22] (further details of IFT are given in the next section). The directed movement of the IFT particles is powered by molecular motors [23–25]. Note that these motors do not appear explicitly in our model; instead, their role in IFT is captured by assigning the corresponding intrinsic velocities of anterograde (tipward) and retrograde (baseward) movement of each IFT particle in the absence of hindrance.

An IFT particle may not be able to move with its intrinsic speed in a dense traffic because of steric hindrance caused by other IFT particles in front of it on the same track. Similar traffic-like collective phenomena in many other subcellular processes (see reference [26–31] for reviews) have been treated in the past as appropriate variants of the totally asymmetric simple exclusion process (TASEP) [32–34]. In the same spirit, the collective movement of the motor-driven IFT particles is represented in our model as a TASEP.

The regulation of transport of the structural proteins by IFT can determine the overall dynamics of the length of a flagellum. The length-dependent regulation of IFT requires feedback based on the flagellar length. Even for a single flagellum, it is challenging to understand how the cell 'knows' or 'senses' the length of its flagellum. Since none of the cells has a 'ruler' for direct measurement of flagellar length, indirect mechanisms are believed to be used by a cell for getting a constant feedback about its flagellar length [35]. Here we present the theoretical formulation of a generic model based on the '*time of flight*' (ToF) mechanism to explore the consequences of such a feedback mechanism on the flagellar length dynamics [35, 36].

The flagellar structural proteins to be transported are loaded as cargoes on the IFT particles; our model explicitly distinguishes between IFT particles and molecular cargoes that the IFT particles transport. Length-sensing by ToF allows a mechanism of '*differential loading*' [37, 38] (see also [39]) of the flagellar structural proteins on the IFT trains at the flagellar base before they begin their anterograde journey. The longer is the flagellum, the fewer incoming IFT trains are loaded with cargoes and the slower is the rate of growth of the flagellum.

We begin with a model for length control of a single flagellum that incorporates all the following key features: (i) a ToF mechanism for length sensing [36], (ii) a mechanism of differential-loading of flagellar structural proteins as cargo on the IFT trains [37, 38], (iii) a TASEP-based representation of the collective traffic-like movement of IFT trains [31], (iv) a flagellar elongation rate that is proportional to anterograde flux of the flagellar structural proteins at the flagellar tip, (v) a flagellar shortening rate that is independent of the flagellar length, but dependent on the extent of IFT density at the flagellar tip, and (vi) synthesis and degradation of flagellar structural proteins in the cell body. Thus, to our knowledge, this is the most comprehensive model of length control of a single flagellum. By a combination of analytical treatment

and computer simulations of both the stochastic and deterministic kinetic equations of this model, we examine the roles of all these ingredients of the model in controlling the length of a single flagellum.

The main aim of this paper, however, is to explore the mechanisms of coordination of the dynamics of the lengths of the two flagella in bi-flagellated eukaryotic cells and their consequences. Our stochastic kinetic model, that retains all the six key features of the model listed above for the kinetics of each individual flagellum, postulates coupling of their dynamics through sharing of the common pool of structural proteins at the base of the flagella. The key differences between our theory and another recently published work [40] on flagellar length control in biflagellates will be discussed later in this paper. Utilizing some of the known properties of TASEP, we present an alternative interpretation of the experimental observations of Ishikawa and Marshall [36]. We show that a ToF mechanism of length regulation is consistent with their experiments. We also predict new results that can, in principle, be tested experimentally.

This paper is organized as follows: in section 2 we present a brief summary of the structure of flagella and the phenomenon of IFT. The ToF mechanism is explained in section 3. The stochastic model for the length control of a single flagellum is formulated in section 4 and the corresponding main results are given in section 5. Experimental supports for the model are claimed in section 6. The model and results for biflagellates are presented in sections 7 and 8, respectively. Detailed comparison of our model with those developed earlier is presented in section 9 thereby highlighting the novel features of our model. Finally, the main conclusions drawn from our model are summarized and suggestions for experimental tests of the new predicted are indicated in section 10.

2. Structure of flagella and intraflagellar transport

2.1. Structure of flagella

Eukaryotic flagella are hair like appendages which emerge from the surface of the cell. The typical length of fully grown flagella in, for example, unicellular algae *C. reinhardtii* (CR) is about $12 \mu\text{m}$. However, various experimental methods have been developed to manipulate the flagellar length [41] that produce even longer or shorter flagella in the steady state.

The structure of a flagellum is based on a cytoskeletal arrangement known as axoneme. It acts both as a scaffold as well as an axle which facilitates beating of the flagellum. The axonemal structure is assembled on a basal body and projects out from the cell surface [42]. The major structural components of all axonemes are microtubule (MT) doublets; each MT being essentially a tubular stiff filament. Each doublet consists of an A-microtubule (A-MT) and a B-microtubule (B-MT). Nine doublet MTs, arranged in a cylindrically symmetric fashion form an axoneme; it extends from the base to the tip. Most axonemes have a $9 + 2$ arrangement of MTs, where nine outer doublets surround a coaxial central pair. Some other axonemes lack a central pair and have a $9 + 0$ arrangement of MTs. The MT doublets are cross-linked by axonemal dynein motors that drive relative sliding of the MT doublets. This sliding, in turn, causes beating of the flagella of eukaryotic cells [43–46].

2.2. Intraflagellar transport (IFT)

In eukaryotic cells an MT serves as a track for two ‘superfamilies’ of cytoskeletal molecular motors, called kinesin and dynein, which move naturally in opposite directions by consuming chemical fuel ATP [23–25]. These motors transport cargo which plays a crucial role not only during growth, but also in the maintenance and shrinkage of flagella [47]. This phenomenon of effective relocation of materials by the active motorized transport machinery is known as intraflagellar transport (IFT) [19, 48, 49]. The crucial role of IFT in the construction of a growing flagellum was established experimentally by demonstrating the obstruction of flagellar growth upon disruption of IFT [21, 50]. Because of their superficial similarities with cargo trains hauled along railway tracks, chain-like assemblies formed by IFT particles are called IFT trains [22, 36, 51, 52]. IFT trains consist of two protein complexes (IFT-A and IFT-B) which have multiple protein–protein interaction domains [53, 54]. The molecular components of the IFT machinery have also been catalogued in detail [55, 56]. More recently, direct evidence for transport of structural proteins and of signalling proteins as cargo of IFT trains has been reported [37, 38, 53]. The different protein–protein interaction domains in the IFT particles allow different cargos hitchhiking on them.

The IFT trains are pulled by motor proteins walking on the MTs that form the axoneme and cycle between the flagellar tip and base [51, 57]. During each leg of their journey the IFT trains remain constrained in the narrow space between the outer surface of the axoneme and the inner surface of the flagellar membrane. IFT-B and kinesin are associated with anterograde transport and only use B-MT for moving from base to the tip. In contrast, IFT-A and dynein participate in the retrograde transport and use

A-MT for moving from tip to the base [52, 58]. However, the number of motors per IFT train is not known. Because of the use of the A-MT and B-MT for moving in opposite directions on an MT doublet, anterograde IFT trains do not collide with the retrograde IFT trains. The IFT particles switch their direction of movement only at the base and the tip of the flagellum. This indicates the plausible existence of a regulatory mechanism for differentially activating and inactivating the appropriate IFT motors at the base and tip to facilitate the directional switching. Recently it has been reported that IFT27 (a component of the IFT train) is responsible for integrating the retrograde machinery (IFT-B complex) into the IFT trains and remodelling of the trains at the tip for the retrograde trip back to the base [58].

Broadly, three different types of proteins perform distinct functions in IFT. Axonemal proteins (mainly tubulins) and other structural proteins are transported as cargoes within flagella. These cargoes are loaded onto IFT particles [37, 38] which are also proteins. Not all IFT particles are loaded with cargo before they begin their journey. Both the empty and loaded IFT particles are hauled along the narrow space between the axoneme and the flagellar membrane by motor proteins that walk along the MT tracks. Since the number of motors per IFT train is not known, we do not describe the motion of the motors explicitly in the model. Instead, the stochastic movement of the IFT trains along the MT tracks are described in terms of kinetic equations.

Why is IFT required in fully grown flagella? This mystery was unveiled when it was observed that there is an ongoing turnover of axonemal proteins at the tip of a fully grown flagellum. Unless replenished by fresh supply of these proteins in a timely manner the flagellum will keep shortening. Therefore, IFT is necessary even in fully grown flagella to maintain the dynamic balance between the rate of growth and disassembly in order to maintain the length at a stationary value [10].

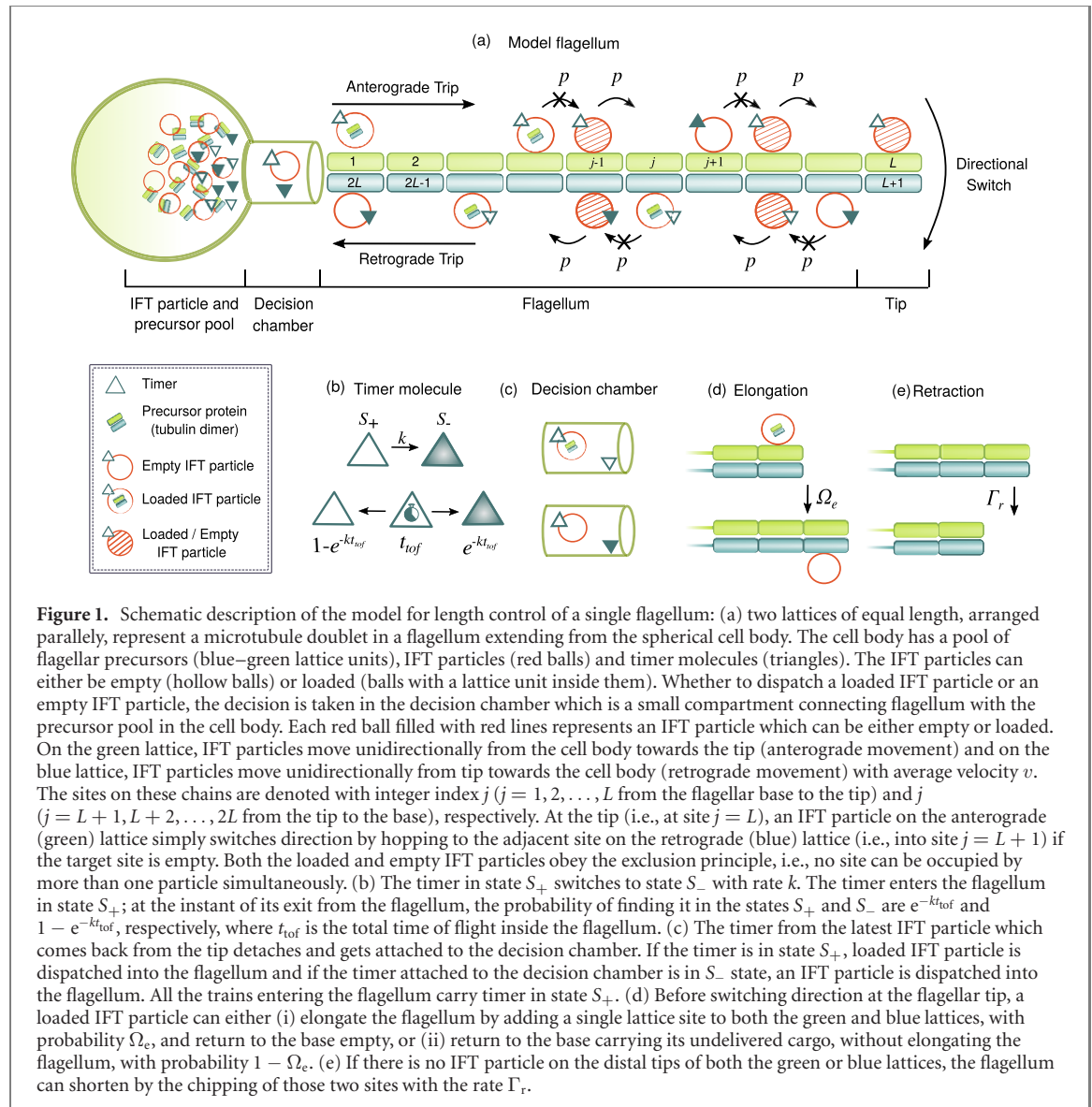
3. Time of flight for measuring length: 'ruler' is a 'timer'

In this brief section we introduce the time-of-flight (ToF) mechanism on which our model of flagellar length control is based [35, 36, 59]. Let us imagine that either the IFT particle itself, or a timer molecule bound to it, is prepared in a specific 'chemical' or 'conformational' state S_+ . The timer enters the flagellum in the state S_+ . However, the state S_+ , being transient, decays spontaneously, and irreversibly, into the state S_- at the rate k . Upon return at the base of the flagellum, the current state of a timer indirectly indicates the length of the flagellum because the longer the flagellum, the longer is the duration of its travel and, hence, the higher is the likelihood of change of its state during the travel. Thus, the 'ruler' used for measuring the length of the flagellum is actually a 'timer'.

The ToF mechanism is based on the idea that, on returning back to the base, the current state of the timer molecule decides whether flagella building material (tubulin) will be loaded onto the IFT particle [37, 38, 60] for the next round of journey. If the timer returns in state S_+ , it indicates a smaller flagellum and directs loading of cargo into the IFT particle departing into the flagellum. On the other hand, the timer returning in state S_- conveys that no more precursor is needed at the flagellar tip for further assembly and allows dispatching of empty IFT particles only. So, only those molecules are suitable for the role of timer whose timescale of switching states is comparable to the time taken by IFT trains to commute around the flagellum [36, 61].

ToF is based on the simple idea that, for a given velocity, the distance travelled is proportional to the time of flight of a particle or a wave. In the context of flagellar length control, a mechanism based on the concept of ToF was formulated first by Marshall and coworkers although the possibility was conjectured by Lefebvre in 2009 [59]. Switching of the state of the timer could be a protein modification like, say, phosphorylation [62]. There are already other examples in molecular cell biology where nature uses the trick of converting time into length. To our knowledge, the most celebrated example is that of the segmentation clock that exploits temporal oscillations to create periodic spatial patterns [63, 64].

Ishikawa and Marshall hypothesised that the timer could be a small GTPase bound to a molecule of GTP as it begins its anterograde journey [36]; the rate of GTP hydrolysis by the GTPase would be the rate k of switching of the timer. Two possible candidates for timer are IFT22 and IFT27 which are components of IFT trains [54]. These small Ras-like GTPases [54, 65] function as switch molecules which cycle between an active GTP-bound form and an inactive GDP-bound form. Huet *et al* [58] investigated the role of IFT27 in *trypanosome* and found that IFT27 enters the flagellum only in GTP-bound state. The cells in which IFT27 is in GTP-locked state, IFT trains enter into the flagellum and build a flagellum of slightly smaller than the normal length flagellum. But, if IFT27 is in GDP-locked state the trains are unable to enter the flagellum thereby preventing its formation. They concluded that the GTP–GDP cycle is essential for maintaining the correct length of the flagellum [58]. For *Chlamydomonas*, it has been reported that partial knocking down of IFT27 affects the elongation of the flagella and a complete knockdown is lethal for the cell [66]. So, these



observations are indications that IFT27 is a possible candidate for timer. But more experiments have to be done to clearly establish whether IFT27 is really a timer that can control the loading of precursor proteins into the IFT trains.

4. Stochastic model for length control of a single flagellum

First we consider the time-dependence of the length of a single flagellum. In this section, we will build the model step by step by clearly justifying all the simplifications. Thereafter, we will formulate the master equations for the qualitative description of our stochastic model and the corresponding Fokker–Planck equation and rate equations.

4.1. Model

The entire elongation and resorption dynamics of a flagellum can be effectively captured by a single MT doublet which, in our model, is represented by two parallel linear chains of equal length L (green and blue lattice chain in figure 1(a)). For the convenience of labelling the sites on these two chains with a single integer index j , the sites on the green (anterograde) chain are labelled by $j = 1, 2, \dots, L$ from the base to the tip and those on the blue (retrograde) chain are labelled by $j = L + 1, L + 2, \dots, 2L$ from the tip to the base. Because of this labelling scheme, the sites $j = L$ and $j = L + 1$ are adjacent to each other at the tips of the two MT tracks for anterograde and retrograde transport, respectively (see figure 1(a)). Each lattice site on both the blue and green lattices represent a tubulin dimer; free dimers in the pool at the base are referred to as precursor proteins.

The precursor proteins are transported as cargoes on IFT trains. Each IFT train is made up of an array of IFT particles. Fusion of IFT particles into IFT trains and fission of IFT trains have been observed experimentally. However, for simplicity, we assume that all the IFT trains consist of a single IFT particle; fusion and fission of the IFT particles do not dominate the phenomena of our interest here. In a flagellum, each IFT train is pulled by several molecular motors. Since the number of motors per IFT train is not known, we do not describe the motion of the motors explicitly in the model. Rather, in our model, each of the self driven hard-core particles (red balls in figure 1(a)) represents a motor-driven single IFT particle; the motors remain implicit. At any given instance, a site of the lattice can be occupied by only one such particle as this mutual exclusion captures the hard-core steric interaction between the IFT particles. An IFT particle at site j moves by hopping to the target site $j + 1$ with rate p if and only if the target site is not occupied by any other IFT particle (see figure 1(a)).

Each IFT train may have the capacity to bind (and carry) multiple cargoes at a time [67]. The IFT particles may be loaded up to maximum capacity during the initial stages of flagellar growth whereas their capacity may remain underutilized in full-length flagella in steady-state [67]. However, for simplicity, we assume that an IFT particle in our model can either be empty (empty red balls in figure 1(a)) or carry one unit for flagellar structural building material (red balls each filled with a precursor in figure 1(a)) which is assumed to be a tubulin dimer (figure 1(a)). The red balls filled by red lines in figure 1(a) denote those IFT particle that can be either empty or loaded with precursor. We have used these to emphasize the ‘exclusion’ principle, i.e., any site occupied by an IFT particle, irrespective of whether or not it is carrying a precursor protein, is not available to the following IFT particle. Moreover, every IFT particle switches its direction of movement, from anterograde to retrograde, at the distal tip of the flagellum.

Whether loaded or empty, every IFT particle that enters the flagellum carries one timer molecule which is in state S_+ (see figure 1(b)). Let the rate at which it can switch stochastically, and irreversibly, to state S_- be k . The master equation for the stochastic process

$$S_+ \xrightarrow{k} S_- \quad (1)$$

is given by

$$\frac{dP_{\text{tm}}^+(t)}{dt} = -kP_{\text{tm}}^+(t) \quad (2)$$

where P_{tm}^+ is the probability density that the timer remain in the state S_+ at time t . The time-dependent solution of (2), corresponding to the given initial condition $P_{\text{tm}}^+(t=0) = 1$, is given by $P_{\text{tm}}^+(t) = e^{-kt}$. Therefore, if the time spent by the timer inside the flagellum is t_{tof} (see figure 1(b)), then the probability P_{tm}^+ that the timer will remain in state S_+ at the moment of its return to the base is given by

$$P_{\text{tm}}^+(t = t_{\text{tof}}) = e^{-kt_{\text{tof}}}. \quad (3)$$

In general, the length covered by an IFT particle during its anterograde journey may not be identical to that covered during its retrograde journey along the same flagellum because of the elongation or shortening of the flagellum during that period. The complete journey of an IFT particle in a fully grown flagellum is of the order of 10 s whereas ciliogenesis requires a time of the order of tens of minutes. Because of this *separation of timescales*, the length of the flagellum remains practically unchanged during the time of a single flight of a timer and its time of flight is taken simply as

$$t_{\text{tof}} = \frac{2L(t)}{v} \quad (4)$$

and, hence, from (3)

$$P_{\text{tm}}^+(t = t_{\text{tof}}) = e^{-2kL(t)/v}. \quad (5)$$

Note also that the average velocity v of the timer (which is identical to that of the IFT particles) depends on the number density (i.e., number per site) ρ of IFT particles in the traffic inside the flagellum. Because of the separation of timescales, we assume that the number density ρ and the flux J of the IFT particles in the flagellum always take corresponding values in the steady-state (time-independent) of the TASEP that represents their traffic. The ρ -dependence of the flux J and mean velocity v in the steady state are given by [32–34]

$$J(\rho) = p\rho(1 - \rho) \quad (6)$$

and

$$v(\rho) = p(1 - \rho) \quad (7)$$

which are fundamental results of TASEP [32–34]. So far TASEP has been applied to understand both vehicular traffic and molecular motor traffic [30, 31].

We assume that whether or not a precursor will be loaded on an IFT particle just before it begins its journey in the flagellum is decided by the state of the timer associated with the latest train to return to the base after shuttling inside the flagellum. In other words, the passengers (precursor proteins) need ‘ticket’ (the state S_+ of the timer) to gain access to the train [68]. This fact is the foundation of the *differential loading model* [37, 38]. In this model, the timer dissociates after completing the retrograde trip and then the timer sticks to the decision chamber (see figure 1(a)). The decision chamber is a hypothetical element connecting the precursor pool and the flagellum which we introduce for our convenience. The immediate neighbourhood of the basal bodies of *Chlamydomonas*, which play several key functions as ‘flagella organizing centres’ [69], is a possible candidate for the decision chamber introduced here. The timer sticks to the decision chamber until the next timer returns back from the tip with the next train. The decision chamber locks the final state of the timer. The final state of the timer then determines the decision of the cell whether to dispatch trains loaded with precursor proteins (if timer is in S_+ state) or just empty train (if the timer is in S_- state) into the flagellum (see figure 1(c)). The timer is then reset into S_+ state and can get utilised by the trains which are about to enter the flagellum (see figure 1(c)).

IFT27, the small GTPases component of the IFT train, detaches from the retrograde IFT trains and remains distributed around the flagellar base [62, 70]. This observation suggests that the flagellar base may be serving as the decision chamber. Moreover, IFT27 only enters the flagellum if in the GTP-bound state. This observation supports our idea that the timer resets to the S_+ state before starting the journey inside the flagellum [58]. When IFT27 is in the GDP bound state, it does not allow the interaction of many proteins with IFT trains and this supports our assumption that when the timer in S_- state no precursor is able to hitchhike the IFT trains which enters the flagellum [58].

Suppose, at the time of entry of IFT particles into the flagellum, the average number of flagellar precursor proteins at the base is $\langle N(t) \rangle$ (the operational meaning of this averaging will be clarified later in this section). The probability of the timer to be in S_+ (stuck to the decision chamber) is given by equation (5). Then, the probability of loading a flagellar precursor onto the IFT particle is

$$\alpha_{tu} = \frac{\langle N(t) \rangle}{N_{\max}} P_{tm}^+(t_{\text{tof}}) = \frac{\langle N(t) \rangle}{N_{\max}} e^{-2kL(t)/v} \quad (8)$$

where N_{\max} denotes the maximum capacity of the precursor protein pool in terms of the number of precursor proteins. In other words, synthesis and degradation of flagellar precursors happen in such a way that the average of the precursor population of the pool does not exceed N_{\max} . This can be achieved by choosing synthesis rate as $\omega^+ [1 - (\langle N(t) \rangle / N_{\max})]$ and degradation rate as $\omega^- \langle N(t) \rangle$. Note that both synthesis and degradation rates depend on the population of precursors in the pool.

If the total flux of IFT particles reaching at the tip is J , then the flux of loaded trains reaching the tip is $\alpha_{tu}J$. On reaching the tip along the anterograde track, a loaded IFT particle can elongate the tracks by one tubulin unit with probability Ω_e and this IFT particle (now empty after delivering its cargo) hops to the newly formed site at the tip of the retrograde lane and begins its return journey to the base (see figure 1(d)). Because of the scheme of labelling the sites on two lattices by a single index, as described above, two extra sites are inserted between the two special sites $j = L$ and $j = L + 1$ thereby increasing the range of j from $1 \leq j \leq 2L$ to $1 \leq j \leq 2L + 2$. Thus, the effective elongation rate of the flagellum is $\alpha_{tu}J\Omega_e$.

In addition to polymerization/elongation mediated by loaded anterograde trains, the axoneme can undergo spontaneous shortening, with the rate Γ_r , by the simultaneous removal of both the sites $j = L$ and $j = L + 1$ at the tip provided both are empty at that instant of time (see figure 1(e)). As the probability of simultaneously finding both the sites empty is $(1 - \rho)^2$ under mean-field approximation, the effective shortening rate is $(1 - \rho)^2\Gamma_r$.

4.2. Master equations for a single flagellum

In this subsection we treat ciliogenesis as a stochastic process where the stochastic kinetics of the length $L(t)$ of the flagellum and that of $N(t)$, the population of the precursors in the common pool, are assumed to be Markovian. Let $P_L(j, t)$ be the probability that the flagellar length at time t is $L(t) = j$. The master equation governing the stochastic kinetics of the flagellar length is given by

$$\frac{dP_L(j, t)}{dt} = \underbrace{\lambda_{j-1, j}^L P_L(j-1, t)}_{\substack{\text{gain by elongation} \\ \text{from } L(t)=j-1 \text{ to } L(t)=j}} + \underbrace{\mu_{j+1, j}^L P_L(j+1, t)}_{\substack{\text{gain by resorption} \\ \text{from } L(t)=j+1 \text{ to } L(t)=j}} - \underbrace{\lambda_{j, j+1}^L P_L(j, t)}_{\substack{\text{loss by elongation} \\ \text{from } L(t)=j \text{ to } L(t)=j+1}} - \underbrace{\mu_{j, j-1}^L P_L(j, t)}_{\substack{\text{loss by resorption} \\ \text{from } L(t)=j \text{ to } L(t)=j-1}} \quad (9)$$

where $\lambda_{j,j+1}^L$ denotes the rate of elongation of the flagellum from state j to $j + 1$ while $\mu_{j,j-1}^L$ denotes that of shortening of flagellar length from state j to $j - 1$.

$$\begin{aligned}\lambda_{j,j+1}^L &= \underbrace{\left[\frac{\langle N(t) \rangle}{N_{\max}} e^{-2kj/v} \right]}_{\alpha_{tu}} J \Omega_e \\ &= \left[\frac{\sum_{n=0}^{N_{\max}} n P_N(n, t)}{N_{\max}} e^{-2kj/v} \right] J \Omega_e\end{aligned}\quad (10)$$

where the expression of α_{tu} is taken from equation (8). Similarly, the rate $\mu_{j,j-1}^L$ of shortening of flagellar length from state j to $j - 1$ is given by

$$\mu_{j,j-1}^L = (1 - \rho)^2 \Gamma_r. \quad (11)$$

Note that, unlike the transition rates $\lambda_{j,j+1}^L$ (equation (10)), $\mu_{j,j-1}^L$ (equation (11)) are independent of j . The crucial consequence of this difference in the j -dependence of λ and μ will be demonstrated by the results that follow from a quantitative analysis.

The precursor synthesis and degradation by the cell, precursor loading onto the IFT particles and addition of precursor chipped from the tip back into pool can change the precursor population from the current state $N(t) = n$ to $n - 1$ or $n + 1$. Let $P_N(n, t)$ denote the probability of finding $N(t) = n$ free precursors in the pool at time t . So, the master equation governing the evolution of the pool population N is given by

$$\begin{aligned}\frac{dP_N(n, t)}{dt} &= \underbrace{\omega^+ \left[1 - \frac{(n-1)}{N_{\max}} \right] P_N(n-1, t) - \omega^+ \left[1 - \frac{n}{N_{\max}} \right] P_N(n, t)}_{\text{population dependent synthesis of flagellar precursor by the cell}} \\ &\quad + \underbrace{[\omega^-(n+1)P_N(n+1, t) - \omega^- n P_N(n, t)]}_{\text{population dependent degradation of flagellar precursor by the cell}} \\ &\quad + \underbrace{\left[\sum_{j=0}^{L_{\max}} J \Omega_e e^{-2kj/v} P_L(j, t) \right] \left[\frac{(n+1)}{N_{\max}} P_N(n+1, t) - \frac{(n)}{N_{\max}} P_N(n, t) \right]}_{\text{contribution of pool towards assembly of the flagellum}} \\ &\quad + \underbrace{(1 - \rho)^2 \Gamma_r [P_N(n-1, t) - P_N(n, t)]}_{\text{precursors returned to the pool by disassembly of the flagellum}}. \quad (12)\end{aligned}$$

The last two terms in (12) have been written under mean-field approximation that ignores correlations between the L and N variables.

As stated earlier, the traffic flow of the IFT particles is represented in our model as a totally asymmetric simple exclusion process (TASEP) [32–34]. Two primary quantities that characterize the steady state of a TASEP are (i) average particle density ρ , and (ii) the average particle flux $J(t)$; these are also the only two properties of TASEP that enter directly in our model through the rates λ^L and μ^L (see equations (10) and (11)). In our numerical plots we will choose values of ρ and J that correspond to one of the three dynamical phases of immediate interest in that analysis (further details are given in the section 6).

To convert the dimensionless length $L(t)$ to actual length (measured in μm) we multiply L with $\delta L = 0.008 \mu\text{m}$, where δL is the size of a single tubulin dimer. To convert the dimensionless flux J (i.e., number of particles per unit time passing through a particular point), velocity v (i.e., the distance covered by an IFT particle per unit time) and the other dimensionless rate constants k, Γ_r, ω^+ and ω^- to actual quantities, we divide them with appropriate δt whose specific values are mentioned in the caption of each figure. The parameter values have been chosen in such a way that the numerical value of the flagellar length in the steady state is about 12 μm , which is comparable to that of each flagellum of *C. reinhardtii*.

4.3. Fokker–Planck equation for a single flagellum

Next we take the continuum limit in which the length of the flagellum is represented by a continuous variable x . In this limit the probability $P_L(j, t)$ reduces to $P_X(x, t)$ which denotes the probability that flagellar length is x at time t . Carrying out the standard Kramers–Moyal expansion of the master equation (9) governing the length of the flagellum, we obtain the corresponding Fokker–Planck equation

$$\frac{\partial P_X(x, t)}{\partial t} = -\frac{\partial}{\partial x} [\{\lambda(x) - \mu(x)\} P_X(x, t)] + \frac{\Delta L}{2} \cdot \frac{\partial^2}{\partial x^2} [\{\lambda(x) + \mu(x)\} P_X(x, t)] \quad (13)$$

where

$$\begin{aligned}\lambda(x) &= \frac{\langle N(t) \rangle}{N_{\max}} J\Omega_e \exp(-2kx/v) \\ \mu(x) &= (1 - \rho)^2 \Gamma_r\end{aligned}\quad (14)$$

and $\Delta L = 1$. The equation (13) describes the stochastic kinetics of the length of the flagellum essentially as a combination of x -dependent drift and diffusion of the flagellar tip where $\lambda(x) - \mu(x)$ and $\lambda(x) + \mu(x)$ are proportional to the effective drift velocity and diffusion constant, respectively.

4.4. Rate equations for a single flagellum

From the master equations for the stochastic time evolution of the length of a single flagellum, we derive the corresponding rate equation (see appendix A for the details)

$$\frac{d\langle L(t) \rangle}{dt} = \underbrace{\left[\frac{\langle N(t) \rangle}{N_{\max}} e^{-2k\langle L(t) \rangle/v} \right]}_{\alpha_{tu}} J\Omega_e - (1 - \rho)^2 \Gamma_r \quad (15)$$

that describes the deterministic time evolution of the mean length

$$\langle L(t) \rangle = \sum_{j=0}^{\infty} j P_L(j, t) \quad (16)$$

of the flagellum. Similarly, from the master equations for population of the precursor pool, we get

$$\frac{d\langle N(t) \rangle}{dt} = \omega^+ \left[1 - \frac{\langle N(t) \rangle}{N_{\max}} \right] - \omega^- \langle N(t) \rangle - \frac{d\langle L(t) \rangle}{dt} \quad (17)$$

which describes the deterministic temporal evolution of the average population of the precursors

$$\langle N(t) \rangle = \sum_{n=0}^{\infty} n P_N(t). \quad (18)$$

5. Results on length control of a single flagellum

5.1. Steady-state of a flagellum: a ‘balance point’

The steady state of the system is defined by the condition $d\langle L(t) \rangle/dt = 0 = d\langle N(t) \rangle/dt$; the corresponding average length of the flagellum and the average population of precursors in the pool are denoted by $\langle L_{ss} \rangle$ and $\langle N_{ss} \rangle$, respectively. From (15), in the steady state, we get $\alpha_{tu} J\Omega_e = (1 - \rho)^2 \Gamma_r$ and using the expression for α_{tu} that follows from equation (8) in the steady-state, we get

$$\langle L_{ss} \rangle = \frac{v}{2k} \log \left[\frac{J\Omega_e}{(1 - \rho)^2 \Gamma_r} \frac{\langle N_{ss} \rangle}{N_{\max}} \right] \quad (19)$$

and

$$\langle N_{ss} \rangle = \frac{\omega^+}{\omega^- + \frac{\omega^+}{N_{\max}}}. \quad (20)$$

For future convenience, we introduce the symbols

$$A = J\Omega_e, \quad (21)$$

$$B = (1 - \rho)^2 \Gamma_r \quad (22)$$

and

$$C = \frac{2k}{v}. \quad (23)$$

In terms of A, B, C , the steady state flagellar length is expressed as

$$\langle L_{ss} \rangle = C^{-1} \log \left[\frac{A}{B} \frac{\langle N_{ss} \rangle}{N_{\max}} \right] \quad (24)$$

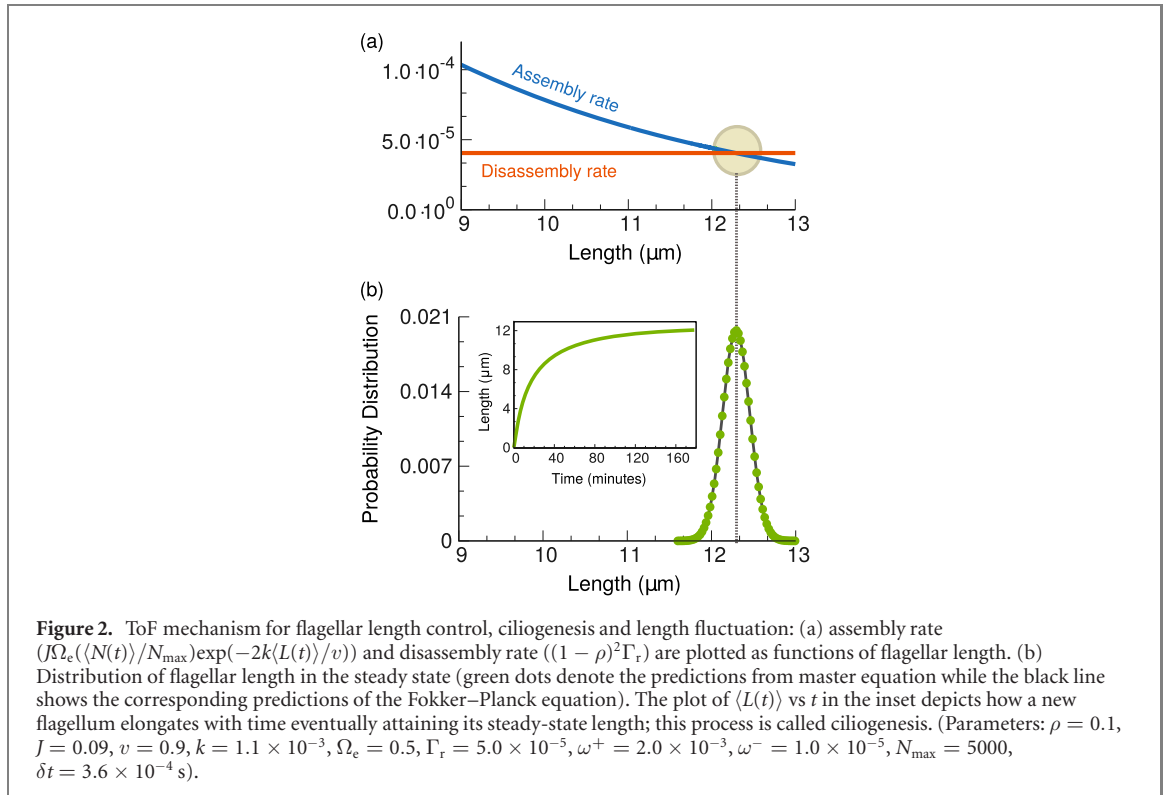


Figure 2. ToF mechanism for flagellar length control, ciliogenesis and length fluctuation: (a) assembly rate ($J\Omega_e(\langle N(t) \rangle / N_{\max}) \exp(-2k\langle L(t) \rangle / v)$) and disassembly rate ($(1 - \rho)^2 \Gamma_r$) are plotted as functions of flagellar length. (b) Distribution of flagellar length in the steady state (green dots denote the predictions from master equation while the black line shows the corresponding predictions of the Fokker-Planck equation). The plot of $\langle L(t) \rangle$ vs t in the inset depicts how a new flagellum elongates with time eventually attaining its steady-state length; this process is called ciliogenesis. (Parameters: $\rho = 0.1$, $J = 0.09$, $v = 0.9$, $k = 1.1 \times 10^{-3}$, $\Omega_e = 0.5$, $\Gamma_r = 5.0 \times 10^{-5}$, $\omega^+ = 2.0 \times 10^{-3}$, $\omega^- = 1.0 \times 10^{-5}$, $N_{\max} = 5000$, $\delta t = 3.6 \times 10^{-4}$ s).

The factor within the square bracket on the right hand side of (19) (or, equivalently, (24)) corresponds to the ratio of the rates of elongation and shortening of the flagellum. However, these rates affect the steady state length of the flagellum only logarithmically. The length of the flagellum is essentially determined by v/k which is a characteristic length set by the ratio of two properties of the timer. Thus, the faster the timer moves (and/or the slower is its conversion to the state S_-) the longer is the magnitude of $\langle L_{ss} \rangle$. In the steady-state the flagellum neither enriches nor depletes the population of the precursors in the pool. The only variation in the population of precursors in the pool arises from the synthesis and degradation of the precursors. Not surprisingly, in large N_{\max} limit, the steady-state population $\langle N_{ss} \rangle$ is determined by the ratio ω^+/ω^- ; the larger is the rate of production (and/or the smaller is the rate of degradation) the higher is the population $\langle N_{ss} \rangle$.

As mentioned in section 4.1, in our model, the effective *assembly* rate $J\Omega_e \exp(-2k\langle L(t) \rangle / v) \langle N(t) \rangle / N_{\max}$ is length-dependent whereas the *disassembly* rate $(1 - \rho)^2 \Gamma_r$ is independent of length. More precisely, the ToF mechanism leads to monotonic decrease of the assembly rate with increasing length; the steady-state is a ‘balance point’ where the assembly rate just balances the rate of disassembly (see figure 2(a)). This result is consistent with the concept of ‘balance-point’ proposed by Rosenbaum, Marshall and others [10, 18, 71].

Because of the intrinsic stochastic nature of the kinetics, as described by the full master equations, the flagellar length $L(t)$ keeps fluctuating around the average length $\langle L_{ss} \rangle$ even in its steady-state. Using the master equation as well as the Fokker Planck equation (see appendices A, B and C for the detailed derivations) we have calculated the steady state distribution that, as shown in figure 2(b), is peaked at $\langle L_{ss} \rangle$. This distribution of the flagellar length in the steady-state is very similar to the distribution of the steady-state lengths of cytoskeletal filaments obtained earlier by following a master equation approach (see, for example, figure 5(c) of reference [72] and figure 2 of [73]).

5.2. Ciliogenesis: controlled assembly of a single flagellum

The process of assembly and disassembly of flagella is referred to as ciliogenesis [74]. All quantitative studies of ciliogenesis normally begin by probing the time-dependent growth of a flagellum. With the same aim, we solved the coupled rate equations (equations (15) and (17)), subject to the initial conditions $\langle L(t=0) \rangle = L(0)$ and $\langle N(t=0) \rangle = N(0)$, respectively, for a set of values of the model parameters; the results are plotted in figure 2(b). The rate of growth of the mean length slows down with time as $\langle L(t) \rangle$ approaches its steady-state value $\langle L_{ss} \rangle$ asymptotically as $t \rightarrow \infty$. This qualitative trend of variation of $\langle L(t) \rangle$ with t is very similar to those observed earlier in experiments [75].

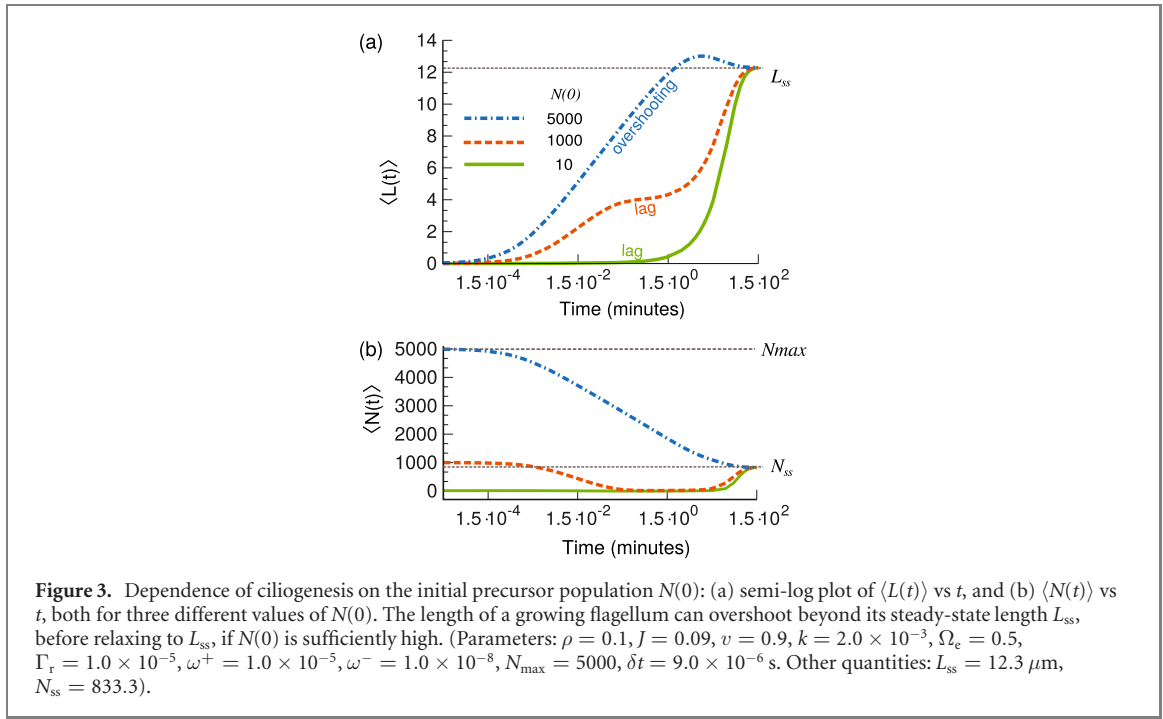


Figure 3. Dependence of ciliogenesis on the initial precursor population $N(0)$: (a) semi-log plot of $\langle L(t) \rangle$ vs t , and (b) $\langle N(t) \rangle$ vs t , both for three different values of $N(0)$. The length of a growing flagellum can overshoot beyond its steady-state length L_{ss} , before relaxing to L_{ss} , if $N(0)$ is sufficiently high. (Parameters: $\rho = 0.1, J = 0.09, v = 0.9, k = 2.0 \times 10^{-3}, \Omega_e = 0.5, \Gamma_r = 1.0 \times 10^{-5}, \omega^+ = 1.0 \times 10^{-5}, \omega^- = 1.0 \times 10^{-8}, N_{\max} = 5000, \delta t = 9.0 \times 10^{-6}$ s. Other quantities: $L_{ss} = 12.3 \mu\text{m}$, $N_{ss} = 833.3$).

Various time scales in the problem have been analysed in appendix D. In the special limiting situation where $\langle N(t) \rangle$ attains steady state value $\langle N_{ss} \rangle$ much faster than $\langle L(t) \rangle$ such that the quantity $N(t)/N_{\max}$ remains practically constant throughout the evolution of the flagellar length, we can approximate the equation (15) by

$$\frac{d\langle L(t) \rangle}{dt} = \left[\frac{\langle N_{ss} \rangle}{N_{\max}} e^{-2k\langle L(t) \rangle/v} \right] J\Omega_e - (1 - \rho)^2 \Gamma_r \quad (25)$$

whose solution is given by

$$\langle L(t) \rangle = \frac{1}{C} \log \left[\frac{N_{ss}}{N_{\max}} \frac{A}{B} - \left(\frac{N_{ss}}{N_{\max}} \frac{A}{B} - e^{CL_0} \right) e^{-BCt} \right] \quad (26)$$

where L_0 is the initial length of the flagellum. From this solution, we conclude that, in this special limit, $\langle L(t) \rangle$ relaxes to its steady-state value $\langle L_{ss} \rangle$ exponentially with the corresponding relaxation time $\tau = 1/(BC)$. In the general case, the correlation between the shapes of the curves $\langle L(t) \rangle$ and $\langle N(t) \rangle$ will be discussed in detail in the next subsection.

5.3. Effects of precursor pool on length of a flagellum

Although the initial amount of precursor $N(0)$ does not affect L_{ss} and N_{ss} , it does affect how steady state is achieved by the flagellar length $L(t)$. In this subsection we systematically study the effects of the time-dependence of $\langle L(t) \rangle$ on $N(0)$. In other words, we systematically explore the interplay of the population kinetics of the precursors $\langle N(t) \rangle$ and growth of the flagellum $\langle L(t) \rangle$ during ciliogenesis. For this purpose, we vary the numerical value of the parameter $N(0)$ over about three orders of magnitude; the values of other model parameters are such that $\langle N_{ss} \rangle \simeq 1000$. We have chosen the interesting regimes of $\omega^+ \gg \omega^-$ and $J\Omega_e \gg \Gamma_r$. We present results for three regimes, namely, $N(0) \gg \langle N_{ss} \rangle$, $N(0) \simeq \langle N_{ss} \rangle$, and $N(0) \ll \langle N_{ss} \rangle$.

In the $N(0) \gg \langle N_{ss} \rangle$ regime the most remarkable observation is that $\langle L(t) \rangle$ can overshoot beyond $\langle L_{ss} \rangle$, before shortening and eventually relaxing to $\langle L_{ss} \rangle$ (see figure 3(a) uppermost curve). As the flagellum grows, and finally relaxes to its steady-state length $\langle L_{ss} \rangle$, the population of the precursors in the pool also relaxes to the corresponding value $\langle N_{ss} \rangle$ (see figure 3(b) uppermost curve). To our knowledge, this effect has not been reported so far in the experimental literature, perhaps, because the value(s) of one or more of the parameters or $N(0)$ in the experiments have never been in the range required to observe this phenomenon.

In the opposite limit $N(0) \ll \langle N_{ss} \rangle$ the most remarkable feature of ciliogenesis is the ‘lag period’. Although the population kinetics of the precursors is switched on at $t = 0$, the growth of the flagellum

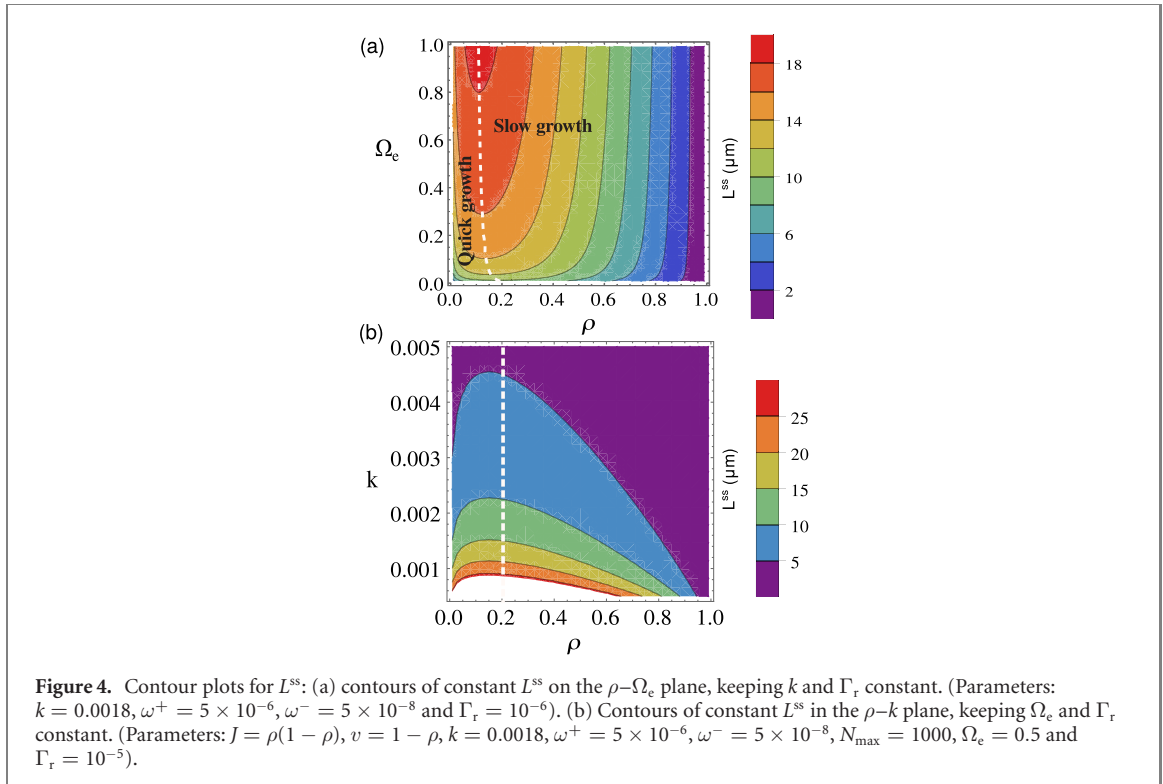


Figure 4. Contour plots for L_{ss} : (a) contours of constant L_{ss} on the $\rho - \Omega_e$ plane, keeping k and Γ_r constant. (Parameters: $k = 0.0018$, $\omega^+ = 5 \times 10^{-6}$, $\omega^- = 5 \times 10^{-8}$ and $\Gamma_r = 10^{-6}$). (b) Contours of constant L_{ss} in the $\rho - k$ plane, keeping Ω_e and Γ_r constant. (Parameters: $J = \rho(1 - \rho)$, $v = 1 - \rho$, $k = 0.0018$, $\omega^+ = 5 \times 10^{-6}$, $\omega^- = 5 \times 10^{-8}$, $N_{\max} = 1000$, $\Omega_e = 0.5$ and $\Gamma_r = 10^{-5}$).

becomes significant only after a ‘lag period’ (see the lowermost curve in figure 3(a)). The precursor population can contribute to sustained growth of the flagellum only after the precursor population in the pool itself begins to rise beyond a critical level (see the lowermost curve in figure 3(b)).

For the intermediate value of $N(0) \simeq \langle N_{ss} \rangle$, initially the flagellar growth exhibits practically no lag period (see the middle curve in figure 3(a)). But, the precursors supplied during this initial growth and those lost by natural decay are not replenished at a comparable rate resulting in a fall in the precursor population (see the middle curve in figure 3(b)). This low population of precursors, in turn, reduces the flagellar growth to almost vanishingly small level (see the middle curve in figure 3(a)). This situation continues, just like the ‘lag period’ discussed before, till fresh synthesis of precursors enlarges the pool population to levels that can resume sustained growth of both the flagellar length as well as its own population, eventually, reaching the steady state (see the middle curves in figures 3(a) and (b)).

5.4. Interplay of traffic, timer and polymerization

As we show in this subsection, the density ρ gives rise to interesting features of the flagellar length dynamics. We have explored the combined effect of ρ , k and Ω_e on the L_{ss} (by using equation (19)) through contour plots. From equations (6), (7) and (19), the dependence of $\langle L_{ss} \rangle$ on ρ , k and Ω_e is given by

$$\langle L_{ss} \rangle = \frac{\rho(1 - \rho)}{2k} \log \left[\frac{\rho \rho \Omega_e}{(1 - \rho) \Gamma_r} \frac{\langle N_{ss} \rangle}{N_{\max}} \right]. \quad (27)$$

For a particular density ρ , a higher value of Ω_e results in a longer L_{ss} (see figure 4(a)). On the other hand, for a fixed value of ρ , L_{ss} decreases with increasing k (see figure 4(b)).

L_{ss} exhibits non-monotonic variation with ρ . For a fixed Ω_e , as we increase ρ , the steady state flagellum length L_{ss} increases with ρ . But for the values of ρ , which lie on the right side of the white-dotted line in the contour plot in figure 4(a), the flagellum length L_{ss} keep on decreasing with increasing ρ . Similar trend is seen in the second contour plot as well (figure 4(b)). When ρ is on the left of the dotted white line (figure 4(b)), with increasing ρ , flux increases which, in turn, increases the supply of precursor at the tip and thus results in longer flagellum with time. On the other hand, when ρ further increases, both the velocity v and the flux J decrease due to congestion of the IFT particles (which can be verified from equations (6) and (7)). Therefore, the timer has to spend more time in the slow-moving congested traffic thereby increasing the probability that it is in the state S_- when it returns to the base. In such situations the timer conveys the wrong message that the flagellum is long enough and prevents additional loading of precursor onto the IFT particles.

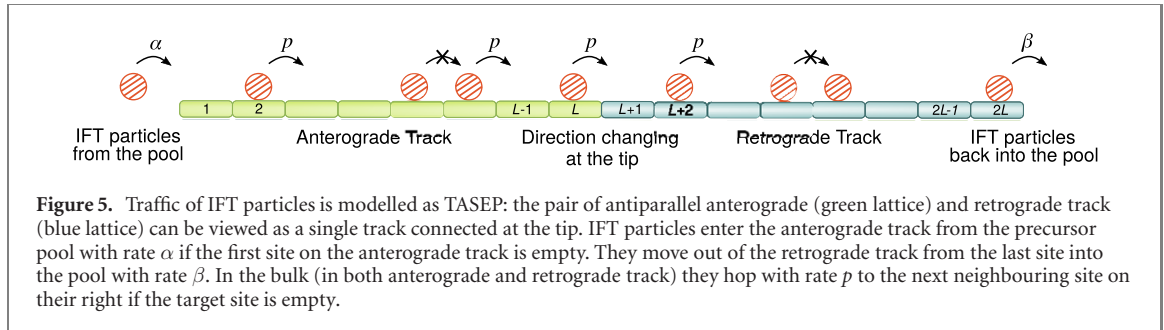


Figure 5. Traffic of IFT particles is modelled as TASEP: the pair of antiparallel anterograde (green lattice) and retrograde track (blue lattice) can be viewed as a single track connected at the tip. IFT particles enter the anterograde track from the precursor pool with rate α if the first site on the anterograde track is empty. They move out of the retrograde track from the last site into the pool with rate β . In the bulk (in both anterograde and retrograde track) they hop with rate p to the next neighbouring site on their right if the target site is empty.

Table 1. Quantities in different phases in TASEP: LD (low density), HD (high density) and MC (maximal current).

Phase	Particle density ρ	Particle flux J	Particle velocity v
LD ($\alpha < \beta, \alpha < \frac{p}{2}$)	$\frac{\alpha}{p}$	$\alpha(1 - \frac{\alpha}{p})$	$p(1 - \frac{\alpha}{p})$
HD ($\beta < \alpha, \beta < \frac{p}{2}$)	$(1 - \frac{\beta}{p})$	$\beta(1 - \frac{\beta}{p})$	β
MC ($\alpha > \frac{p}{2}, \beta > \frac{p}{2}$)	$\frac{p}{2}$	$\frac{p}{4}$	$\frac{1}{2}$

The properties of the TASEP, that represents the traffic of IFT particles, also provides a means of testing the ToF hypothesis. The ToF mechanism works satisfactorily provided the average velocity of the IFT trains remains practically constant. However, if for any reason the rate of entry of the IFT particles onto the anterograde track exceeds a limit imposed by TASEP, the IFT particles may find themselves in the high-density phase in which the IFT particles would take a very long ToF and would erroneously signal against loading of the IFT particles with tubulins. Consequently, the HD phase of the TASEP would result in a shorter than usual L_{ss} .

6. Experimental supports for the model

The adoption of the TASEP for modelling the intraflagellar traffic of IFT particles is a key new ingredient of our model. We summarize here the key features of TASEP, particularly in the context of IFT, before detailed discussion on the interpretation of experimental results from the perspective of TASEP. Irrespective of its load status, an anterograde IFT particle hops to the next site in the forward direction with the rate p only if the target site is empty. Similarly, a retrograde IFT particle hops with the rate p to the target site only if the latter is empty. Thus, the traffic flow of the IFT particles is modelled as a totally asymmetric simple exclusion process (TASEP) [47–49]. This process is completely characterised by three parameters (see figure 5): α (rate with which a particle hops into the lattice at one end), β (rate with which a particle hops out of the lattice at the other end) and p (rate with which a particle hops into its nearest neighbour lattice site if the target site is empty). The three primary quantities that completely characterize the steady state of such processes are (i) average particle density ρ (or, more precisely, the density profile), (ii) the average particle flux J and (iii) the mean particle velocity v which is defined as the average total number of sites hopped per unit time. The three different (non-equilibrium) phases can be realized on the track in the steady state of the system: (i) sparsely crowded low density (LD) phase, (ii) highly crowded high density (HD) phase and (iii) a phase with the optimal flow known as maximal current (MC) phase. The primary quantities as a function of α, β and p in three different phases are summarised in table 1.

The density ρ of the IFT particles depends on the dynamical phase, i.e., whether the traffic of the IFT particles is in the LD, HD or the MC phase. We consider the IFT particle traffic to be always in the LD phase. In the LD phase, if we have the number density $\rho(\alpha, \beta, p) = \rho$, the corresponding flux J and mean velocity v are unique and can be expressed as a function of ρ only. The flux and the mean velocity are given by (6) and (7), respectively.

6.1. Experimental test for the validities of ToF mechanism and TASEP for IFT

A set of experiments was carried out by Ishikawa and Marshall [36] to test the validity of the ToF mechanism. In *C. reinhardtii* cells with mutant dyneins the retrograde transport was slower than that in wild type cells, as expected. But, contrary to their expectation, Ishikawa and Marshall [36] observed that the slowing down of the retrograde IFT lead to an increase in the flux of the anterograde IFT, instead of a decrease. Based on their interpretation of the data, they believed that their observations ‘rule out the

time-of-flight mechanism as a means of controlling injection as a function of length'. But, what was missing in their analysis for the interpretation of the data is the role of the principles of TASEP. By re-interpreting their data in this subsection, in the light of the properties of TASEP, we argue that their observation is, contrary to their conclusion, fully consistent with our ToF-based model developed in this paper.

Like shuttle trains, IFT trains cycle between the base and the tip of a flagellum. In our model so far the times for anterograde and retrograde travel were considered to be equal although, in reality, the velocities of the IFT particles in the two directions are almost certainly different. Moreover, after reaching the tip of the flagellum, kinesin-driven IFT particles do not immediately begin their dynein-driven retrograde journey. Instead, upon arrival at the flagellar tip, a train detaches from the anterograde track (B-microtubule), spends some time τ at the tip in an unattached state during which it gets 'remodelled' [76], then attaches to the retrograde track (A-microtubule) after which it starts moving towards the base from the tip [51]. During remodelling a loaded IFT particle may unload the cargo (tubulin precursors), an empty IFT particle may get loaded with turned over structural protein, unbind (or deactivate) kinesins and activate dyneins (which are carried as cargo by the anterograde IFT trains).

In order to explain their key experimental observations, the generalized expression for the time of flight (t_{tof}) inside the flagellum considered by Ishikawa and Marshall [36] was

$$t_{\text{tof}} = \underbrace{(L/v_a)}_{\text{time of travel from base to tip}} + \underbrace{(L/v_r)}_{\text{time of travel from tip to base}} + \underbrace{\tau}_{\text{time spent at the tip for remodelling}}. \quad (28)$$

Accordingly, the equation (8) would get generalized to

$$\alpha_{\text{tu}} = \frac{\langle N(t) \rangle}{N_{\text{max}}} e^{-k\{(L/v_a) + (L/v_r) + \tau\}} \quad (29)$$

where v_a and v_r are the average velocities of IFT particles in the anterograde and retrograde directions, respectively. The equation (29) implies that any decrease in the retrograde velocity v_r of the IFT particles would cause decrease of α_{tu} , i.e., probability of loading of the tubulin into the IFT particles. This observation is consistent with Ishikawa and Marshall's comment that their experimental observations on the increase of the flux of anterograde particles 'do not rule out the possibility that a time-of-flight scheme might regulate cargo loading' [36].

Following Ishikawa and Marshall [36], the concept of remodelling time τ has been introduced in equation (29) only for the sake of completeness of our discussion. But, in our actual calculation we have used $\tau = 0$ and incorporated its effect indirectly through effective rates β_{eff} and α_{eff} (see figure 6) which we have obtained self-consistently by imposing steady-state condition on the flux. The assumption of steady-state condition, in turn, is justified by the fact that neither accumulation nor depletion of IFT particles with passage of time have been observed so far in any experiment.

Next, we assign different hopping rates to the anterograde and retrograde IFT particles, thereby mimicking different average velocities of the IFT particles in the anterograde and retrograde directions. In such situations where the rates of hopping of the IFT particles in the anterograde and retrograde transport are unequal, the TASEP effectively becomes a composite of two TASEPs in the two distinct segments that are coupled at the tip of the flagellum. As shown in figure 6(a), β_{eff} is the effective rate of exit of the IFT particles from the first segment (anterograde transport) while α_{eff} is the effective rate of entry of the IFT particles into the second segment (retrograde transport).

As stated in section 4, in the steady-state each TASEP can exist in one of the three possible dynamical phases, namely, LD, HD and MC. Thus, for a composite TASEP, as in figure 6(a), the phase of the system in the steady state can be denoted by the symbol $\mathcal{P}_A|\mathcal{P}_R$ where \mathcal{P}_A and \mathcal{P}_R refer to the phases of the anterograde and retrograde segments, respectively. Naively, it may appear *a priori* that the system can exist in nine distinct composite phases $\mathcal{P}_A|\mathcal{P}_R$ where each of \mathcal{P}_μ ($\mu = A$ or R) can be in LD, or HD or MC phase. Since the same steady state flux has to be sustained in both the segments, not all of the nine phases are physically realizable. Only those composite phases are stable which can maintain a single steady flux through the entire composite system. The physical implications of this principle will be established in this section.

Let us begin our discussion here with the simplest situation $p_A = 1.0 = p_R = p$. Moreover, we select $\alpha = 0.1$ and $\beta = 1.0$ so that α is rate limiting. Under this condition, the TASEPs in both the segments (i.e., on anterograde and retrograde direction) are in LD phase, i.e., the composite phase is LD|LD. The resulting average density of the IFT particles in both the anterograde and retrograde segments is $\rho_A = \alpha/p = \rho_R$ and the corresponding flux is $J_A = \alpha(1 - (\alpha/p)) = J_R$ (see the curves corresponding to $p_R = 1.0$ in figures 6(b) and (c)).

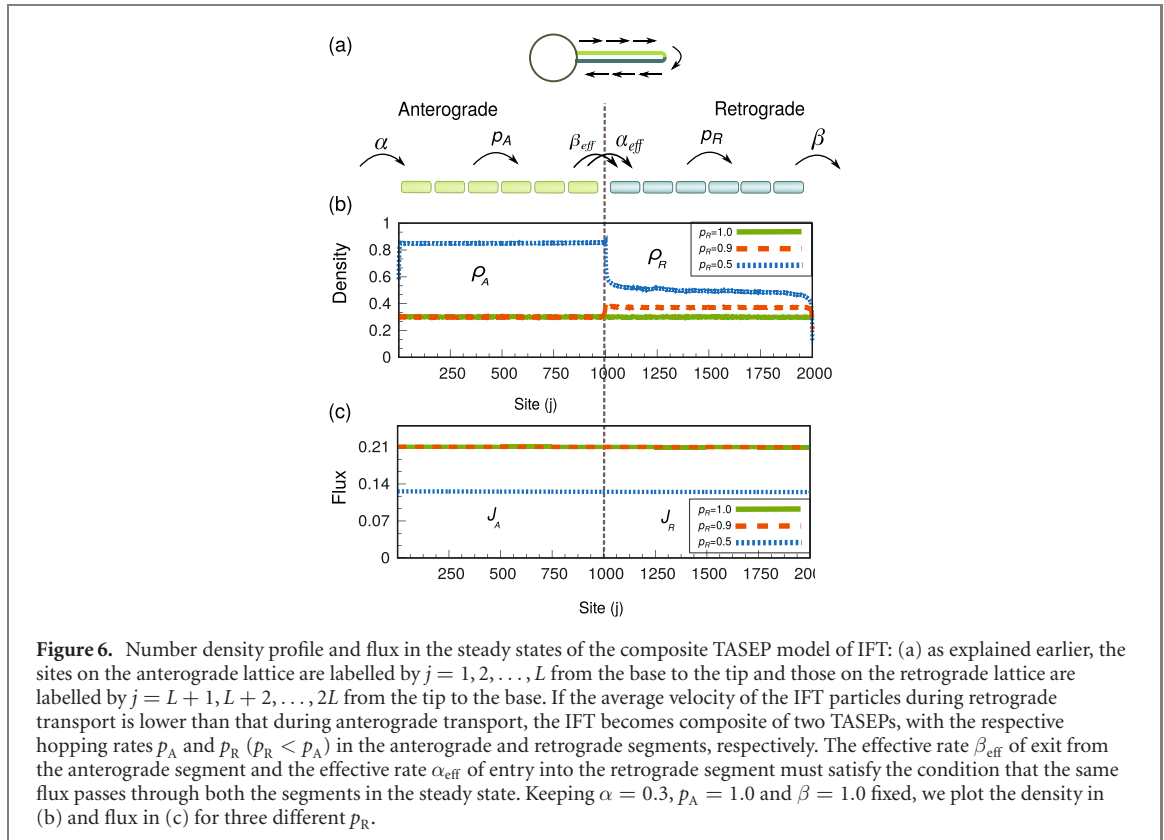


Figure 6. Number density profile and flux in the steady states of the composite TASEP model of IFT: (a) as explained earlier, the sites on the anterograde lattice are labelled by $j = 1, 2, \dots, L$ from the base to the tip and those on the retrograde lattice are labelled by $j = L + 1, L + 2, \dots, 2L$ from the tip to the base. If the average velocity of the IFT particles during retrograde transport is lower than that during anterograde transport, the IFT becomes composite of two TASEPs, with the respective hopping rates p_A and p_R ($p_R < p_A$) in the anterograde and retrograde segments, respectively. The effective rate β_{eff} of exit from the anterograde segment and the effective rate α_{eff} of entry into the retrograde segment must satisfy the condition that the same flux passes through both the segments in the steady state. Keeping $\alpha = 0.3$, $p_A = 1.0$ and $\beta = 1.0$ fixed, we plot the density in (b) and flux in (c) for three different p_R .

As p_R decreases, without change in the value of p_A , the densities ρ_A and ρ_R in the two segments change in such a way that the condition $J_A = J_R$ continue to be satisfied by the two steady-state fluxes J_A and J_R in the anterograde and retrograde directions. Expressing J_A and J_R in terms of p_A , p_R and the unknown α_{eff} , we get the equation

$$\alpha(1 - (\alpha/p_A)) = \alpha_{eff}(1 - (\alpha_{eff}/p_R)) \quad (30)$$

whose solution yields

$$\alpha_{eff} = \frac{p_A p_R - \sqrt{p_A p_R} \sqrt{4\alpha^2 - 4\alpha p_A + p_A p_R}}{2p_A}. \quad (31)$$

From (31), we find that when p_R is decreased, α_{eff} remains real as long as $p_R > p_R^*$, with

$$p_R^* = \frac{(4\alpha p_A - 4\alpha^2)}{p_A} \quad (32)$$

is satisfied. In such situations, both the segments are in their respective LD phases and the composite system is still in the LD|LD phase although $\rho_A \neq \rho_R$ because $\alpha \neq \alpha_{eff}$ (see the curves corresponding to $p_R = 0.9$ in figures 6(b) and (c)).

However, if

$$p_R < p_R^* \quad (33)$$

the retrograde segment cannot sustain the anterograde flow. The flux in both the segments is controlled by p_R which is now rate limiting. If the condition (33) is satisfied, the retrograde segment is in the MC phase while the anterograde segment is in the HD phase so that the composite system exhibits the HD|MC phase (see the curves corresponding to $p_R = 0.5$ in figures 6(b) and (c)). So, now the steady-state condition in terms of the equality of the fluxes J_A and J_R gives

$$\beta_{eff}(1 - (\beta_{eff}/p_A)) = p_R/4 \quad (34)$$

whose solution gives the expression

$$\beta_{eff} = \frac{1}{2}(p_A - \sqrt{p_A^2 - p_A p_R}) \quad (35)$$

Table 2. Steady state properties of composite two-TASEP model.

Condition	$J_A = J_R = J$	ρ_A
$p_R > \frac{(4\alpha p_A - 4\alpha^2)}{p_A}$	$\alpha(1 - (\alpha/p_A))$	α/p_A
$p_R < \frac{(4\alpha p_A - 4\alpha^2)}{p_A}$	$p_R/4$	$1 - \beta_{\text{eff}}$

for β_{eff} . The average IFT particle density in anterograde segment is now given by

$$\rho_A = 1 - \beta_{\text{eff}} \quad (36)$$

while the corresponding flux is $J_A = p_R/4$. The condition, in terms of p_R , and the corresponding anterograde density and common flux are summarized in table 2.

The results plotted in figures 6(b) and (c) correspond to a specific value of α . In order to illuminate the role of α , we plot ρ_A , ρ_R and $\rho_A - \rho_R$ in figure 7 as functions of p_R , keeping $p_A = 1.0 = \beta$ fixed. For every given value of α the system exhibits the composite phase LD|LD for all $p_R > p_R^*$; although ρ_A remains unaffected, ρ_R continues to increase with the decrease of p_R because of the corresponding change of α_{eff} . Exactly at $p_R = p_R^*$ the system makes a transition to the composite phase HD|MC where ρ_A increases by a discontinuous jump and ρ_R attains its maximum value. With further decrease of p_R , ρ_A continues to increase while ρ_R now remains unaffected.

The most interesting point here is that, for a given α , $\rho_A - \rho_R$ changes sign at $p_R = p_R^*$ so that for $p_R < p_R^*$, $\rho_A > \rho_R$. The higher values of ρ_A for $p_R < p_R^*$ than the value for $p_R > p_R^*$ is consistent with the higher intensity observed by Ishikawa and Marshall [36] in the case of IFT with mutant dyneins. We believe that the ‘injection intensity’ that Ishikawa and Marshall [36] claimed to have measured in their experiment is actually proportional to the average density, rather than flux, of the IFT particles in the anterograde segment.

With the above interpretation of the experimental observations and comparison with our theoretical predictions, we establish that both the (i) time-of-flight mechanism for length control, and (ii) description of the traffic of IFT particles in terms of TASEP are consistent with experimental observations [36].

6.2. Role of depolymerases in the ‘balance-point’ scenario

By a series of experiments, Pan and coworkers [77–79] established the following facts:

- Flagellar shortening requires the depolymerases to the extent that the shortening is inhibited in depolymerase-depleted cells.
- In the steady state, the depolymerases are almost exclusively located in the cell body and very little traces of it are found in the flagella. However, when flagellar shortening is triggered by internal cues or external signals, the depolymerases are rapidly transported to the flagellar tip where these begin depolymerization of the axonal MTs.
- Since the depolymerases in CR do not possess the domains required for active motor-like walk towards the plus-end of the MTs, the only plausible mode of their rapid transport to the flagellar tip is as cargo on anterograde IFT that are driven by other families of processive kinesin motors.

In our model, continuation of turnover of the tubulins in the steady-state requires depolymerization rate to be non-zero (as for the disassembly rate-1 in figure 8). However, shortening of the flagella during resorption can occur in two different ways. In the first, the polymerization probability Ω_e can be switched off, without altering the depolymerization rate Γ_r , thereby triggering resorption (see figure 9). In the second, the depolymerization rate Γ_r increases abruptly, without any change in the polymerization probability Ω_e (see figure 10) thereby shifting the balance points to a shorter length [3] as shown in figure 8. In the latter case if the shifted balance point still corresponds to a non-zero length, the flagella shorten, but resorption is only partial (as for the disassembly rate-2 in figure 8). But, if the increase of Γ_r is sufficiently large, the resulting shift of the balance points can be so large that the steady-state corresponds to vanishing length of the flagella indicating complete resorption (as for the disassembly rate-3 in figure 8). This scenario of depolymerase-induced resorption is consistent with the experimental observations of Pan and co-workers [77, 78], but quite different from the length-dependent depolymerization proposed recently in reference [40]. The mechanisms of flagellar length control that we have postulated in this paper are also different from that, proposed for control of length of microtubules, based on a length-dependent feedback on polymerization by kinesin Kip2 [80].

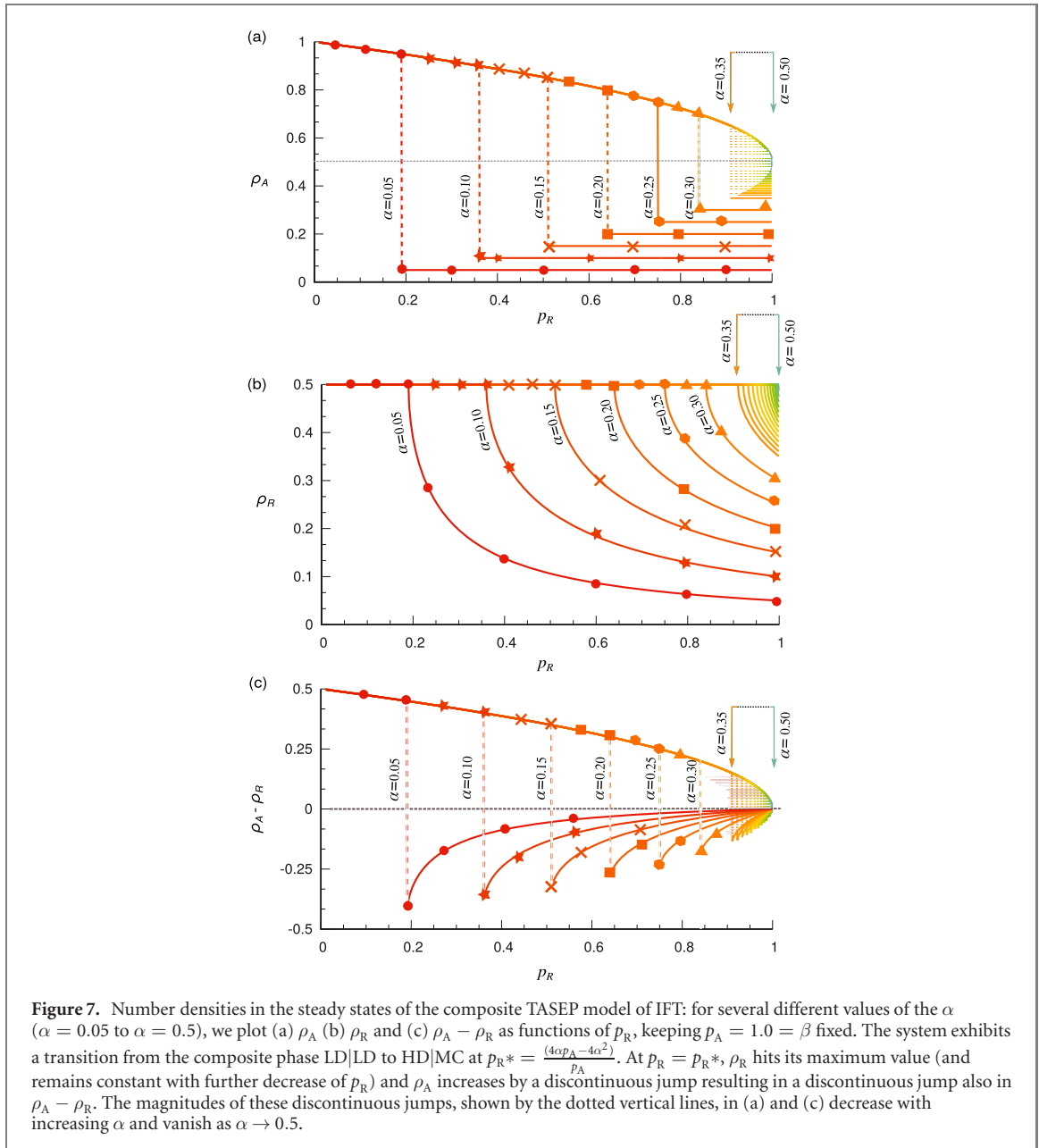


Figure 7. Number densities in the steady states of the composite TASEP model of IFT: for several different values of the α ($\alpha = 0.05$ to $\alpha = 0.5$), we plot (a) ρ_A (b) ρ_R and (c) $\rho_A - \rho_R$ as functions of p_R , keeping $p_A = 1.0 = \beta$ fixed. The system exhibits a transition from the composite phase LD|LD to HD|MC at $p_R^* = \frac{(4\alpha p_A - 4\alpha^2)}{p_A}$. At $p_R = p_R^*$, ρ_R hits its maximum value (and remains constant with further decrease of p_R) and ρ_A increases by a discontinuous jump resulting in a discontinuous jump also in $\rho_A - \rho_R$. The magnitudes of these discontinuous jumps, shown by the dotted vertical lines, in (a) and (c) decrease with increasing α and vanish as $\alpha \rightarrow 0.5$.

7. Stochastic model for length control in biflagellates

In the preceding section we have developed a model for length control of a single flagellum. Analyzing that model and comparing its predictions with known empirical facts, we have established the validity of the hypotheses on which the model is based. In this section we couple two such model flagella to develop a theoretical model for flagellar length control in biflagellates. The emphasis of this section is in the study of cooperative effects of the coupling.

In addition to all the simplifications listed above for the dynamics of a single flagellum, we make one more simplification regarding the coupling of the dynamics of the two flagella in a biflagellate. The dynamics of the two flagella are coupled via the common pool of flagellar protein precursors at the base; we consider explicitly only the tubulins, the building blocks of axonemal MTs, in this pool because those are the most dominant component in it. The flagella are also assumed to share a common pool of IFT particles. That is why the same flux J of IFT trains appears in the master equations of the two flagella. A timer molecule returning to the base upon completion of a round trip in a flagellum dwells in the decision chamber providing the feedback required for the differential loading of an IFT train that is poised to begin its next journey. Thereafter the timer goes back to the pool at the base, gets re-charged and waits for the next hitch-hiking on another IFT train.

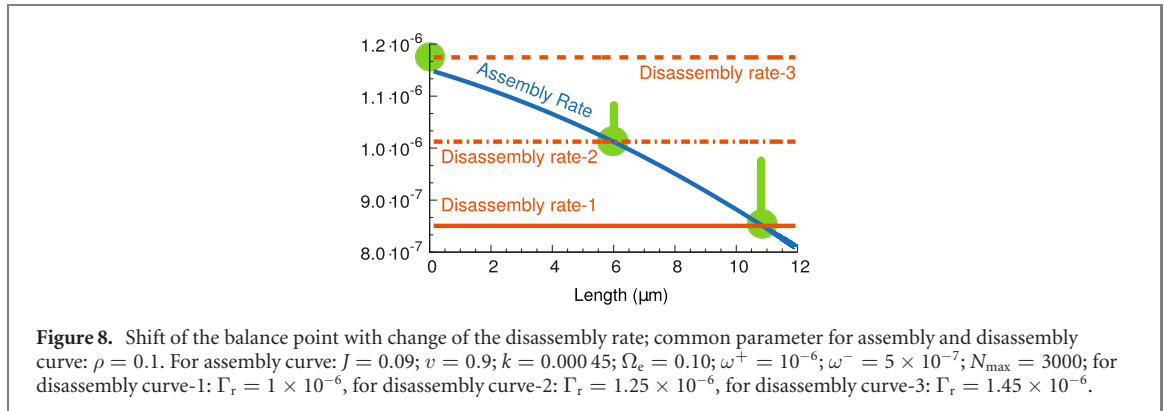


Figure 8. Shift of the balance point with change of the disassembly rate; common parameter for assembly and disassembly curve: $\rho = 0.1$. For assembly curve: $J = 0.09$; $v = 0.9$; $k = 0.00045$; $\Omega_e = 0.10$; $\omega^+ = 10^{-6}$; $\omega^- = 5 \times 10^{-7}$; $N_{\max} = 3000$; for disassembly curve-1: $\Gamma_r = 1 \times 10^{-6}$, for disassembly curve-2: $\Gamma_r = 1.25 \times 10^{-6}$, for disassembly curve-3: $\Gamma_r = 1.45 \times 10^{-6}$.

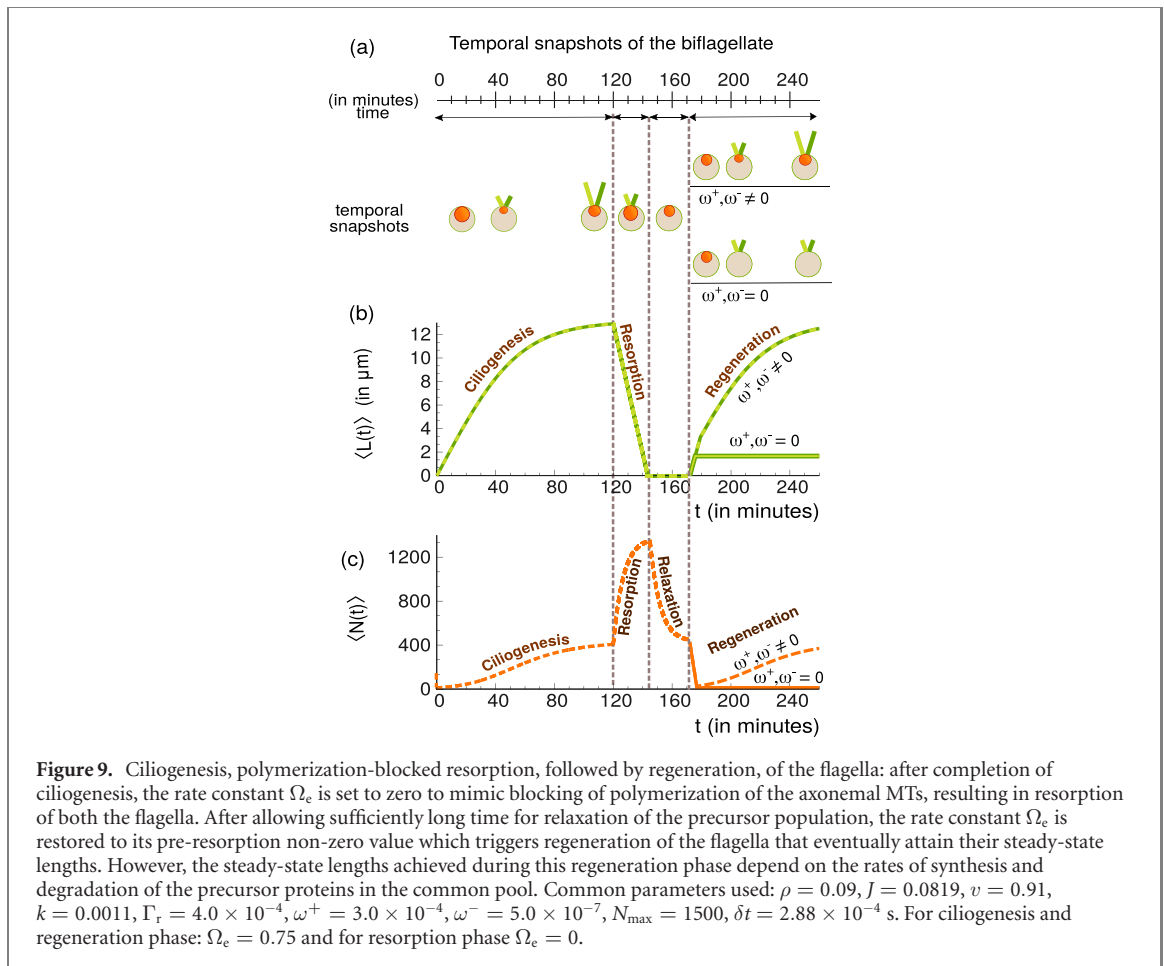


Figure 9. Ciliogenesis, polymerization-blocked resorption, followed by regeneration, of the flagella: after completion of ciliogenesis, the rate constant Ω_e is set to zero to mimic blocking of polymerization of the axonemal MTs, resulting in resorption of both the flagella. After allowing sufficiently long time for relaxation of the precursor population, the rate constant Ω_e is restored to its pre-resorption non-zero value which triggers regeneration of the flagella that eventually attain their steady-state lengths. However, the steady-state lengths achieved during this regeneration phase depend on the rates of synthesis and degradation of the precursor proteins in the common pool. Common parameters used: $\rho = 0.09$, $J = 0.0819$, $v = 0.91$, $k = 0.0011$, $\Gamma_r = 4.0 \times 10^{-4}$, $\omega^+ = 3.0 \times 10^{-4}$, $\omega^- = 5.0 \times 10^{-7}$, $N_{\max} = 1500$, $\delta t = 2.88 \times 10^{-4}$ s. For ciliogenesis and regeneration phase: $\Omega_e = 0.75$ and for resorption phase $\Omega_e = 0$.

7.1. Master equations for a biflagellate

Let $P_{L_1}(j, t)$ ($P_{L_2}(j, t)$) be the probability that the length of flagellum f_1 (f_2) at time t is $L_1(t) = j$ ($L_2(t) = j$). The master equation governing the stochastic kinetics of the length of flagellum f_1 and f_2 , given in appendix E, are appropriate generalizations of the master equations for a single flagellum.

7.2. Rate equations for length control in biflagellates

The equations governing the evolution of average length $\langle L_1(t) \rangle$ and $\langle L_2(t) \rangle$ of flagellum f_1 and f_2 are

$$\begin{aligned} \frac{d\langle L_1(t) \rangle}{dt} &= \left[\frac{\langle N(t) \rangle}{N_{\max}} e^{-2k\langle L_1(t) \rangle/v} \right] J\Omega_e - (1 - \rho)^2 \Gamma_r \\ \frac{d\langle L_2(t) \rangle}{dt} &= \left[\frac{\langle N(t) \rangle}{N_{\max}} e^{-2k\langle L_2(t) \rangle/v} \right] J\Omega_e - (1 - \rho)^2 \Gamma_r \end{aligned} \quad (37)$$

and the equations governing the evolution of the average precursor population $\langle N(t) \rangle$ in the pool is

$$\frac{d\langle N(t) \rangle}{dt} = \omega^+ \left[1 - \frac{\langle N(t) \rangle}{N_{\max}} \right] - \omega^- \langle N(t) \rangle - \frac{d\langle L_1(t) \rangle}{dt} - \frac{d\langle L_2(t) \rangle}{dt}. \quad (38)$$

8. Results on length control of a biflagellate

8.1. Ciliogenesis, resorption and subsequent regeneration

CR cells lose their flagella by one of the two well known mechanisms called (i) *resorption*, and (ii) deflagellation [9]. During the process of *resorption* a flagellum is gradually retracted into the cell. In contrast, *deflagellation* refers to the process of shedding of the flagella that involves severing of the entire flagellum from its base [16]. In this subsection we present results obtained from our model for the process of resorption, and subsequent regeneration of the flagella. Our results for the process of deflagellation will be presented in the next subsection.

The plot of lengths $\langle L_1(t) \rangle$ and $\langle L_2(t) \rangle$ of the two flagella is the simplest, and most direct, way of presenting the empirical data on ciliogenesis. The slope of each of the curves at a given time t indicates the rate $V_1(t)$ and $V_2(t)$, respectively, of elongation of the corresponding flagella at that instant of time. In most of the systems the rates $V_1(t)$ and $V_2(t)$ decrease with increasing t and eventually, after a time interval T , vanish as the flagella attain their steady-state lengths $\langle L_1^{\text{ss}} \rangle$ and $\langle L_2^{\text{ss}} \rangle$. These qualitative features of the experimental data are captured very well by the numerical results obtained by solving the rate equation (37), together with the equation (38) for the given initial conditions $\langle L_1(0) \rangle = 0 = \langle L_2(0) \rangle$, $\langle N(0) \rangle = N_0$ (see figure 9). The rate constants have been tuned so as to obtain $\langle L_1^{\text{ss}} \rangle = 12 \mu\text{m} = \langle L_2^{\text{ss}} \rangle$, which is the typical length of the flagella of wild type CR in the steady-state [36].

8.1.1. Resorption in our model: a plausible scenario

In our numerical studies of the model we mimicked the resorption process by setting the term $[\frac{\langle N(t) \rangle}{N_{\max}} e^{-2k\langle L_1(t) \rangle/v}]J\Omega_e$ to zero which implies either the rate $\Omega_e = 0$ (vanishing of elongation rate), or $J = 0$ (vanishing rate of flux of the IFT trains), or $e^{-2k\langle L_1(t) \rangle/v} = 0$ (vanishing rate of tubulin loading). In that situation, because of the nonvanishing Γ_r , the lengths of both the flagella keep decreasing till both $\langle L_1(t) \rangle = \langle L_2(t) \rangle \rightarrow 0$, manifesting as the phenomenon of *resorption* as shown in figures 9(a) and (b).

Note that during resorption none of the structural proteins constituting the flagella are lost by the cell; instead, those are actually returned to the basal pool [9, 16]. Suppose resorption begins when the system is in the steady state. If the synthesis and degradation of the structural proteins were blocked as the resorption begins, then at the end of resorption the net population of structural proteins in the pool would have been $\langle N^{\text{ss}} \rangle + \langle L_1^{\text{ss}} \rangle + \langle L_2^{\text{ss}} \rangle$. However, if the synthesis and/or degradation of the structural proteins are not blocked and the resorption is not sufficiently rapid, then $N_{\text{df}} \neq \langle N^{\text{ss}} \rangle + \langle L_1^{\text{ss}} \rangle + \langle L_2^{\text{ss}} \rangle$ where N_{df} is the population of structural proteins in the pool at the moment of completion of resorption.

If $[\frac{\langle N(t) \rangle}{N_{\max}} e^{-2k\langle L_1(t) \rangle/v}]J\Omega_e$ remains zero for sufficiently long time even after disappearance of the two flagella, the population of the precursors in the common pool relaxes to the new steady-state corresponding to $\Omega_e = 0$. This *relaxation* of the precursor pool population is also shown in figure 9(c).

Resorption does not remove the basal bodies [81]. Therefore, the same basal bodies remain available for regeneration of the flagella. If the elongation rate Ω_e is again switched on at this stage, the *regeneration* of the two flagella proceed in a manner qualitatively similar to that during ciliogenesis (see figure 9) and both flagella eventually regain the respective original steady-state lengths $\langle L_1^{\text{ss}} \rangle = 12 \mu\text{m} = \langle L_2^{\text{ss}} \rangle$.

Rosenbaum *et al* [75] found that if CR were deflagellated in cycloheximide, a known inhibitor of protein synthesis, then upon regeneration the flagella can attain only a length of about $6 \mu\text{m}$ whereas the normal full length of flagella in CR is about $12 \mu\text{m}$. This result established that the CR cells maintain a pool of the essential structural proteins that can be exploited for regeneration of flagella. But, in the absence of fresh synthesis of these proteins, the existing pool is not adequate for regeneration upto the full length of $12 \mu\text{m}$. This feature is also reproduced by our model, as depicted in figures 9(a) and (b).

8.1.2. An alternative scenario of resorption in our model

Based on a series of experiments, Pan and collaborators [15, 77, 78] have suggested that shortening of the flagella, which requires depolymerization of the axonemal MTs, is dominantly driven by MT depolymerases which belong to distinct families of kinesin motors [82–84]. Those experiments also indicated that under normal conditions the population of the depolymerases in the flagella is negligibly small. However, upon receiving a specific signal, depolymerases rush into the shaft of a flagellum and quickly reach the distal tips of the MTs where they begin MT depolymerization at a high rate.

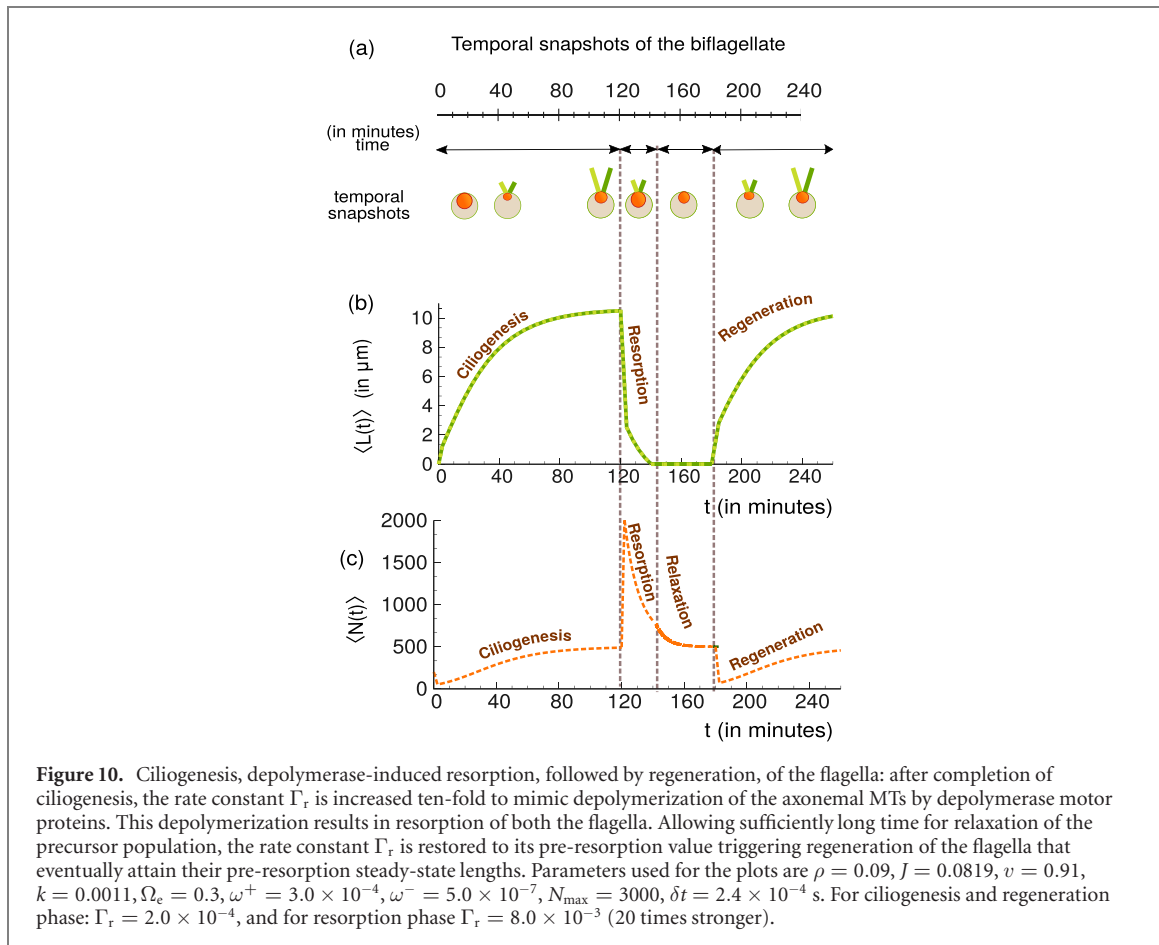


Figure 10. Ciliogenesis, depolymerase-induced resorption, followed by regeneration, of the flagella: after completion of ciliogenesis, the rate constant Γ_r is increased ten-fold to mimic depolymerization of the axonemal MTs by depolymerase motor proteins. This depolymerization results in resorption of both the flagella. Allowing sufficiently long time for relaxation of the precursor population, the rate constant Γ_r is restored to its pre-resorption value triggering regeneration of the flagella that eventually attain their pre-resorption steady-state lengths. Parameters used for the plots are $\rho = 0.09$, $J = 0.0819$, $v = 0.91$, $k = 0.0011$, $\Omega_e = 0.3$, $\omega^+ = 3.0 \times 10^{-4}$, $\omega^- = 5.0 \times 10^{-7}$, $N_{\max} = 3000$, $\delta t = 2.4 \times 10^{-4}$ s. For ciliogenesis and regeneration phase: $\Gamma_r = 2.0 \times 10^{-4}$, and for resorption phase $\Gamma_r = 8.0 \times 10^{-3}$ (20 times stronger).

In order to establish that our model is capable of capturing the experimentally indicated role of depolymerases in resorption, we abruptly implemented a ten-fold increase of the rate Γ_r well after the flagella attained their steady-state values L^{ss} , without altering the numerical value of the growth term $[\frac{\langle N(t) \rangle}{N_{\max}} e^{-2k\langle L_1(t) \rangle/v}]J\Omega_e$. The abrupt increase of Γ_r causes resorption. However, allowing sufficient time for relaxation to the new steady-state, if the numerical value of the parameter Γ_r is restored to its pre-resorption value, the two flagella again regain their pre-resorption lengths L^{ss} through regeneration process. For this case, the evolution of flagellar length and pool population are shown in figures 10(a)–(c).

8.2. Flagellar dynamics after deflagellation and subsequent regeneration

When subjected to environmental stress like, for example, extreme temperatures or pH or presence of detergents or alcohols in the medium [17, 18, 85], a CR cell itself severs its flagella so that each flagellum abruptly shortens to a length $f\langle L^{ss} \rangle$ where $f = 0$ corresponds to shedding of the entire flagellum. That is why deflagellation is also referred to as flagellar excision, flagellar shedding or flagellar autotomy [16]. The dynamics of regeneration of flagella after deflagellation need not be identical to those after resorption because the structural proteins that constitute the severed part of a flagella are lost by the cell during deflagellation whereas the structural proteins are gradually retracted into the common pool during resorption.

In the *in-silico* experiments with our model, we mimicked deflagellation by abruptly, and instantaneously, reducing the lengths of each of the two flagella to a shorter value $f\langle L^{ss} \rangle$ where $0 \leq f < 1$ without altering the numerical value of any of the model parameters. The data for $f = 0$ and $f = 1/2$ are plotted in figures 11(a)–(c). Immediately after the deflagellation, the existing pool has to provide the much needed initial resources for the regeneration of the flagella. Consequently, in the immediate aftermath of severing of the flagella, the population $\langle N(t) \rangle$ of the precursors in the pool decreases (see figure 11). However, in the mean time, enhanced synthesis of the flagellar components begins; these freshly synthesized proteins not only replenish the depleted pool but also become available for the continued growth of the flagella. IFT particles moving inside a flagellum at the instant of amputation also get lost. But this loss of IFT particles has negligible effect because the pool of IFT particle is generally quite large and only a small

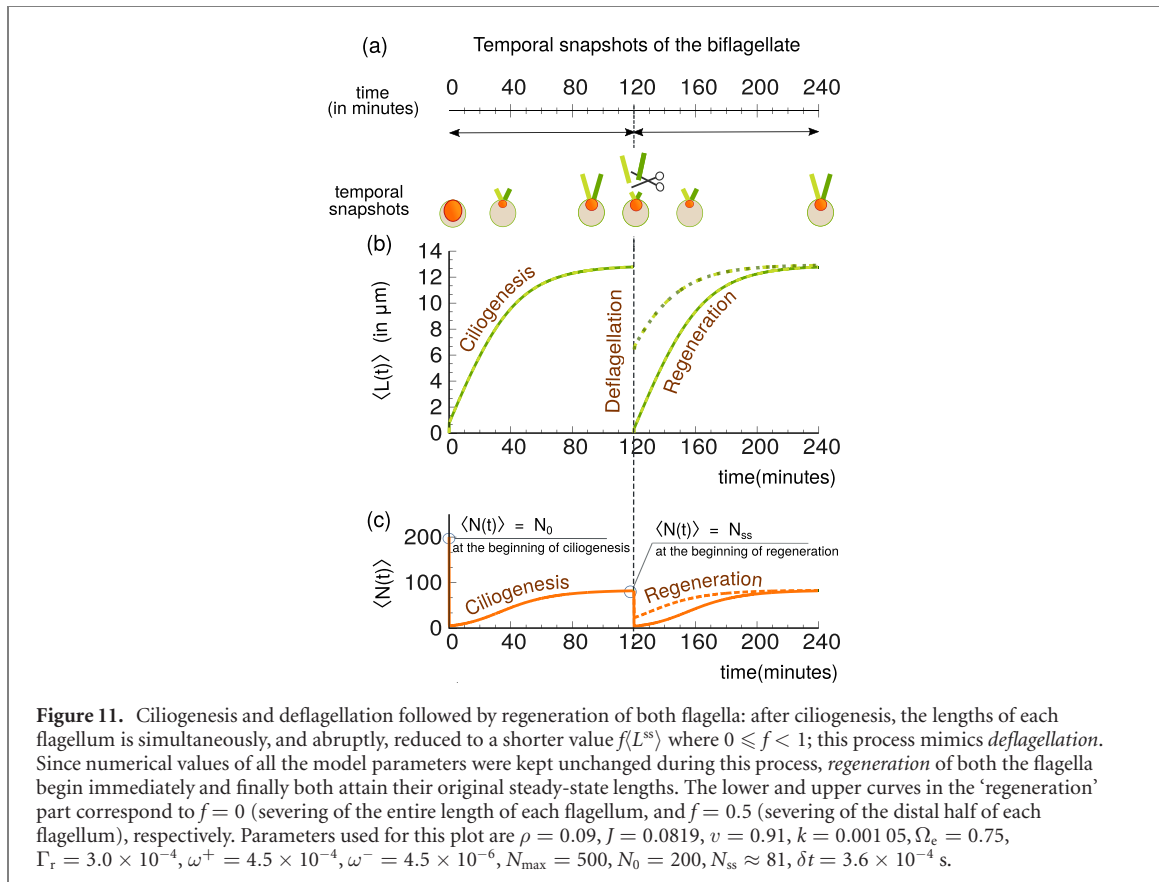


Figure 11. Ciliogenesis and deflagellation followed by regeneration of both flagella: after ciliogenesis, the lengths of each flagellum is simultaneously, and abruptly, reduced to a shorter value $f\langle L^{ss} \rangle$ where $0 \leq f < 1$; this process mimics deflagellation. Since numerical values of all the model parameters were kept unchanged during this process, regeneration of both the flagella begin immediately and finally both attain their original steady-state lengths. The lower and upper curves in the ‘regeneration’ part correspond to $f = 0$ (severing of the entire length of each flagellum, and $f = 0.5$ (severing of the distal half of each flagellum), respectively. Parameters used for this plot are $\rho = 0.09$, $J = 0.0819$, $v = 0.91$, $k = 0.00105$, $\Omega_e = 0.75$, $\Gamma_r = 3.0 \times 10^{-4}$, $\omega^+ = 4.5 \times 10^{-4}$, $\omega^- = 4.5 \times 10^{-6}$, $N_{\max} = 500$, $N_0 = 200$, $N_{ss} \approx 81$, $\delta t = 3.6 \times 10^{-4}$ s.

fraction of IFT particles participate in shuttling inside the flagellum (roughly 20%) [55, 86]. Both the flagella and the population of the precursors in the common pool eventually attain their respective original steady-state values irrespective of the value of f .

8.3. Flagellar dynamics after selective amputation and subsequent regeneration

In the context of deflagellation, discussed above, both the flagella were severed to equally shorter lengths. In this subsection we consider the more general case where the two flagella are severed unequally. We refer to this process as selective amputation in order to distinguish it from the process of deflagellation. For simplicity, we consider the scenario where one of the two flagella is selectively severed to a length $f\langle L^{ss} \rangle$ ($0 \leq f < 1$) while the other flagellum remains intact, the special case of this situation corresponding to $f = 0$ is usually referred to as ‘long-zero case’.

The curiosity-driven exploration of the consequences of amputation of flagella of unicellular eukaryotes began almost seventy years ago when regeneration of severed flagella was first observed [87]. The first quantitative study of the kinetics of regrowth of the shortened flagella was reported soon thereafter [88]. Since then the mechanisms of flagellar length regulation under wide varieties of conditions and chemo-physical perturbation have been investigated with many species of flagellated eukaryotes using several different experimental techniques with increasing sophistication [41]. In their pioneering works Rosenbaum and coworkers [75, 81, 89, 90] used either paralysed strains or applied compression through a coverslip to hold the cells under study for direct viewing (see, for example, [75]). Both types of perturbations are likely to affect the objects and processes of interest in this context. In recent times, ingenious experimental methods have been developed that avoid possible adverse effects on the normal physiology of the flagellated cells under investigation [91]. All those experiments helped in collecting wealth of information not only on the regeneration of the severed flagellum but also on the effects of this selective amputation and regeneration on the length of the unsevered flagellum.

In the ‘long-zero case’, the unsevered flagellum is found to resorb rapidly while the severed one begins to elongate. When the resorbing unsevered flagellum and the regenerating amputated flagellum attain the same length, both elongate at the same rate till regaining their original (equal) steady-state lengths. In principle, a cell could sense the damage/amputation of a flagellum by the loss of a function that crucially depends on the undamaged full-length normal flagellum. However, a paralysed flagellum, which is disabled to perform its function of driving fluid flow, can still regenerate upon amputation [91]. This experimental

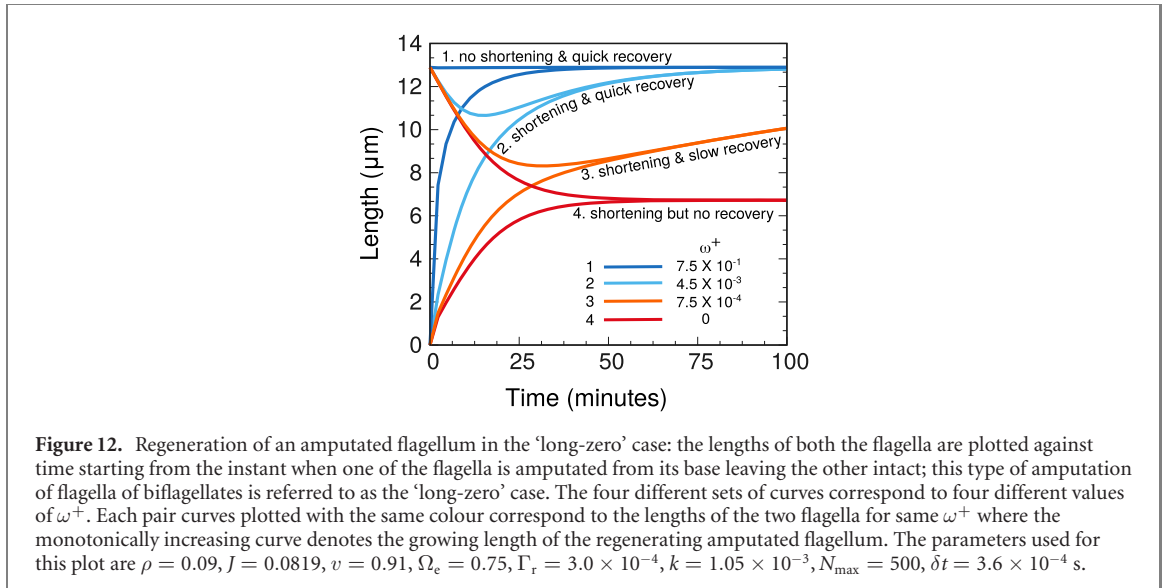


Figure 12. Regeneration of an amputated flagellum in the ‘long-zero’ case: the lengths of both the flagella are plotted against time starting from the instant when one of the flagella is amputated from its base leaving the other intact; this type of amputation of flagella of biflagellates is referred to as the ‘long-zero’ case. The four different sets of curves correspond to four different values of ω^+ . Each pair curves plotted with the same colour correspond to the lengths of the two flagella for same ω^+ where the monotonically increasing curve denotes the growing length of the regenerating amputated flagellum. The parameters used for this plot are $\rho = 0.09$, $J = 0.0819$, $v = 0.91$, $\Omega_e = 0.75$, $\Gamma_r = 3.0 \times 10^{-4}$, $k = 1.05 \times 10^{-3}$, $N_{\max} = 500$, $\delta t = 3.6 \times 10^{-4}$ s.

evidence indicates that the ‘loss-of-function’ is neither a mode of sensing damage/amputation of a flagellum nor the stimulus for fresh synthesis of the flagellar proteins by the cell. Therefore, how the unsevered flagellum senses the amputation of its partner and how it responds to this perturbation by initiating own resorption remains one of the challenging open questions on this phenomenon.

We mimicked the long-zero amputation and subsequent regeneration in our model by choosing the initial conditions $\langle L_1(0) \rangle = \langle L_1^{ss} \rangle$, $\langle L_2(0) \rangle = 0$, $\langle N(0) \rangle = \langle N^{ss} \rangle$. The flux J of IFT particles in the two flagella is same because both the flagella share the same pool of IFT particles and amputation of one flagellum does not affect the overall population of IFT particles in the pool [55, 86]. The data for four different values of ω^+ are plotted in figure 12. The qualitative trend of variation of $\langle L_1(t) \rangle$ and $\langle L_2(t) \rangle$ for the two intermediate values of ω^+ are consistent with the empirically observed facts; for both the unsevered flagellum shortens initially till equalization of its length with the elongating severed partner and then the two flagella grow together to full recovery. The flagellar proteins released by the shortening flagellum is utilized by the elongating flagellum during the early stages of the latter’s regeneration [89]. Subsequently, unless suppressed by inhibitors, fresh synthesis of flagellar proteins provides the material needed for full growth of the two flagella to their pre-amputation original lengths.

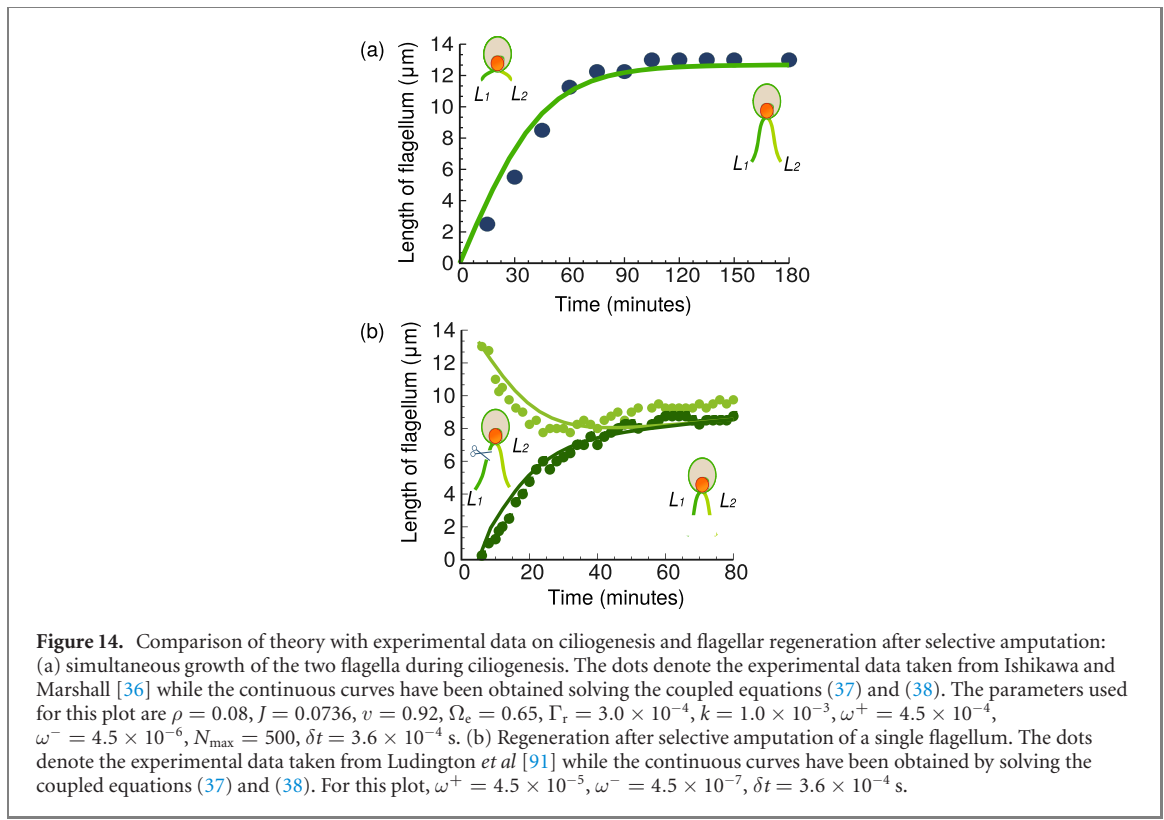
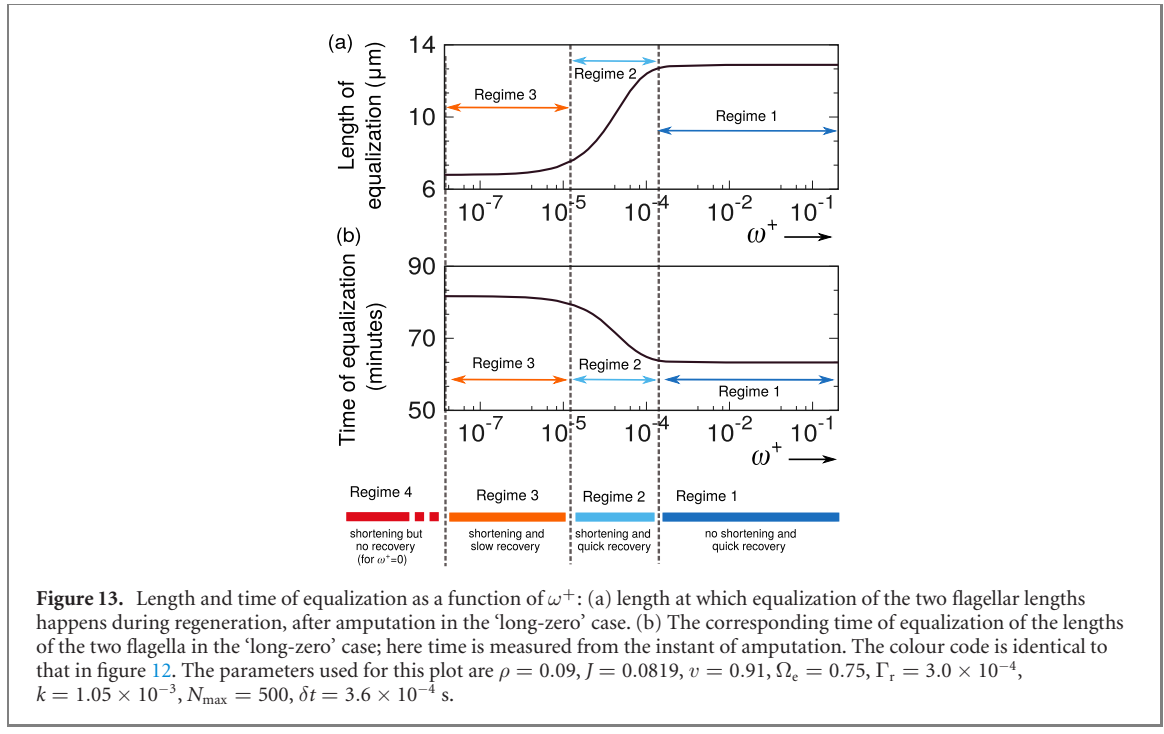
Moreover, the larger is the numerical value of ω^+ the quicker is the recovery. In fact, in the case of the highest value of ω^+ used in figure 12, the recovery of the amputated flagellum is so quick that practically no shortening of the unsevered flagellum is observed. On the other hand, in the opposite extreme case where $\omega^+ = 0$, only the unsevered flagellum supplied the structural proteins required for the growth of the amputated flagellum; consequently, both the flagella can attain a steady-state length of only $L^{ss}/2 \simeq 6 \mu\text{m}$, as observed earlier experimentally. Thus, the nature of the kinetics of regeneration of the amputated flagellum depends on the kinetics of synthesis of the precursor proteins in the common pool (see figure 13).

We tested whether the model explains the experimental observation i.e., the elongation/resorption pattern of the amputated/unamputated flagellum of the CR as reported by Ludington *et al* [91] and Ishikawa and Marshall [36]. For this purpose, we selected numerical values of all the parameters to get the best fit between the experimental data [36] and our theoretical prediction of the time-dependence of flagellar lengths during ciliogenesis (see figure 14(a)). Then, using the same numerical values of all the parameters, except ten times smaller values of ω^+ and ω^- , we could get excellent fit to our theory and the experimental data on the time-dependence of the flagellar lengths following amputation in the long-zero case (see figure 14(b)).

8.4. Beyond mean: fluctuations and correlation

For the numerical computation of the correlations, we begin with the following definitions: suppose, the total number of realizations generated is n . Let $L_1^i(t)$ and $L_2^i(t)$ denote the length of flagellum-1 and 2 at time t in i th realization. The instantaneous *mean* lengths of the two flagella are defined by

$$\langle L_1(t) \rangle = \frac{\sum_{i=1}^n L_1^i(t)}{n}, \quad \text{and} \quad \langle L_2(t) \rangle = \frac{\sum_{i=1}^n L_2^i(t)}{n}, \quad (39)$$



while the corresponding *variances* are given by

$$\begin{aligned} \text{Var}(L_1) &= \left[\frac{1}{n-1} \sum_{i=1}^n (\langle L_1(t) \rangle - L_1^i(t))^2 \right]^{1/2} \\ \text{Var}(L_2) &= \left[\frac{1}{n-1} \sum_{i=1}^n (\langle L_2(t) \rangle - L_2^i(t))^2 \right]^{1/2} \end{aligned} \quad (40)$$

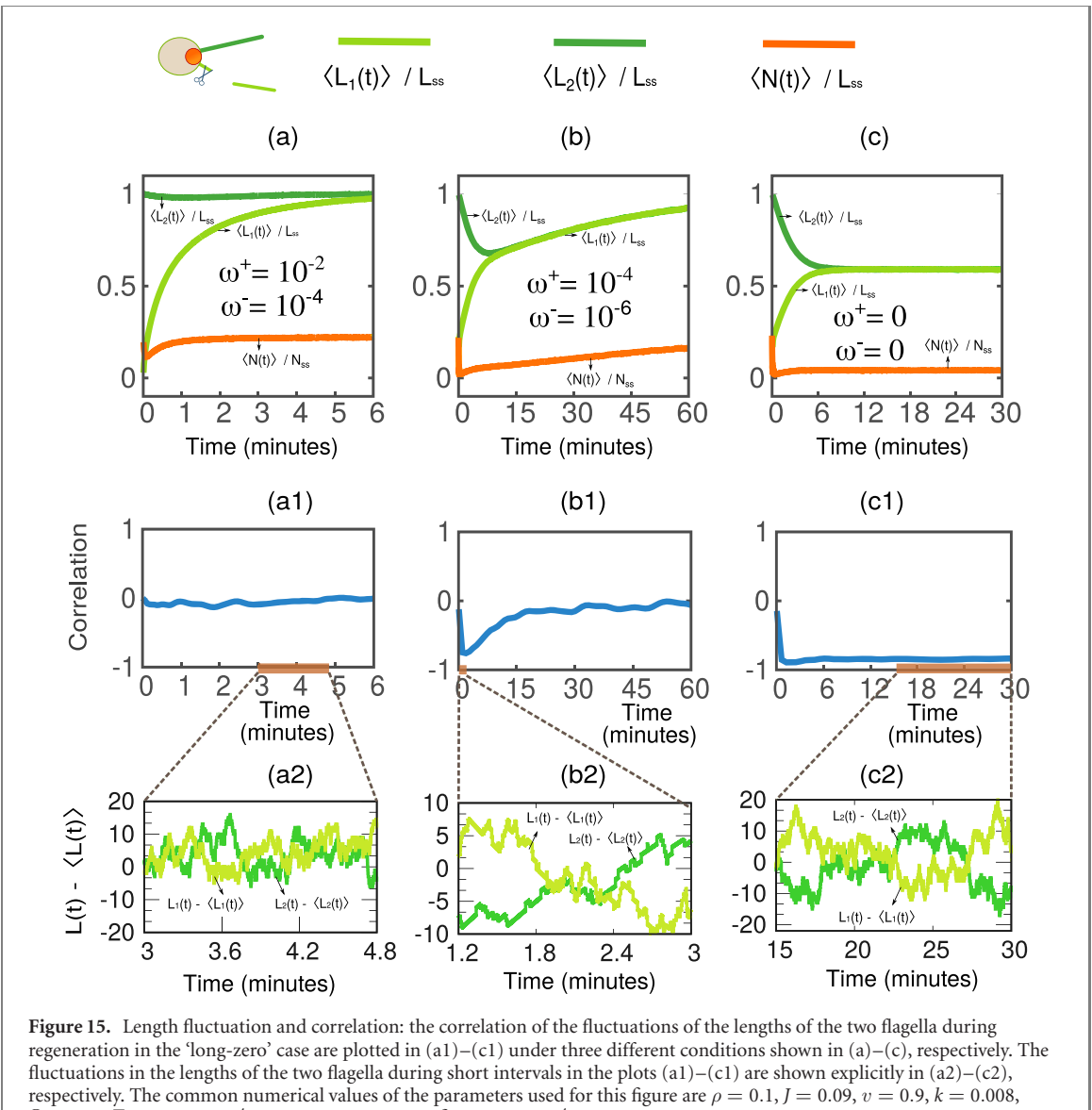


Figure 15. Length fluctuation and correlation: the correlation of the fluctuations of the lengths of the two flagella during regeneration in the ‘long-zero’ case are plotted in (a1)–(c1) under three different conditions shown in (a)–(c), respectively. The fluctuations in the lengths of the two flagella during short intervals in the plots (a1)–(c1) are shown explicitly in (a2)–(c2), respectively. The common numerical values of the parameters used for this figure are $\rho = 0.1$, $J = 0.09$, $v = 0.9$, $k = 0.008$, $\Omega_e = 0.5$, $\Gamma_r = 5.0 \times 10^{-4}$, $N_{\max} = 100$, $N_0 = 50$, $\delta t = 3.6 \times 10^{-4}$ s.

and the covariance $\text{Cov}(L_1 L_2)$ is given by

$$\frac{1}{n-1} \left[\sum_{i=1}^n (\langle L_1(t) \rangle - L_1^i(t)) (\langle L_2(t) \rangle - L_2^i(t)) \right]^{1/2}. \quad (41)$$

In terms of these variances and the covariance, the correlation between the flagellar lengths is defined as

$$\text{Corr}(L_1 L_2) = \frac{\text{Cov}(L_1 L_2)}{\text{Var}(L_1) \text{Var}(L_2)}; \quad (42)$$

and it gives a quantitative measure of the correlation of fluctuations in the lengths of the two flagella. Then a set of n realizations of stochastic trajectories are generated by simulating the model using Monte-Carlo methods as described in appendix F.

We studied the $\text{Corr}(L_1 L_2)$ for three different cases: (i) negligibly small resorption of the unsevered flagellum before equalization of its length with that of regenerating flagellum (figure 15(a)), (ii) significant shortening of the unsevered flagellum till equalization of the lengths of the two, followed by recovery of pre-amputation steady-state lengths of both (figure 15(b)) and (iii) significant shrinkage of the unsevered flagellum till both the flagella attain a steady-state length of $\approx L^{\text{ss}}/2$ and stop growing further (figure 15(c)).

In the case (i), the correlation remained zero throughout the regeneration process (see figure 15(a1)). Since the proteins required for the regeneration of the amputated flagellum are supplied exclusively by the precursor pool, leaving the unamputated flagellum practically unaffected, there is no correlation between the length fluctuations of the two flagella (see figure 15(b1)).

In case (ii), the correlation exhibited a nonmonotonic behaviour; starting from the initial value zero, it became negative and its absolute value increased with the passage of time till it attained its minimum beyond which it increased gradually to its final value zero (see figure 15(a2)). The correlation was found to be negative during the initial period when the shortening unamputated flagellum made significant contribution to the supply of proteins that sustained the regeneration of the amputated flagellum. This fact is demonstrated clearly by the plots in figure 15(b2)).

In case (iii), the correlation became negative as soon as the amputated flagellum started growing at the expense of the unamputated flagellum and remained negative throughout, even after both the flagella attained their new steady lengths (see figure 15(c1)). Since in this case synthesis and degradation of the precursors were blocked, any increase of the length of one of the two flagella had to be compensated by the corresponding decrease in the length of the other, i.e., the fluctuations in the lengths of the two flagella were always anti-correlated. This is clearly visible in figure 15(c2)).

From all these three cases it could be concluded that the correlation between the fluctuation of lengths of the flagellum is strongly related to the precursor population in the pool. Actually, through this precursor pool both the flagellum interact. When sufficient precursor is present in the pool to support the regeneration of the amputated flagellum, the correlation is vanishingly small (figures 15(a)–(a2)). But, during those time intervals when the precursors get depleted, then one flagellum grows at the cost of other, leading to negative correlation (figures 15(b)–(b2)). And in those extreme situations where one flagellum can grow only at the expense of the other, correlation remains negative for the whole time (figures 15(c)–(c2)).

9. Comparison with other models

A summary of all the known theoretical models of flagellar length control and critical analysis of their implications was reported few years ago by Ludington *et al* [35]. Several of those models could be ruled out through their systematic analysis. But, some others, which could not be discarded by the experimental evidence, still remain as plausible, although alternative, scenarios for flagellar length control. One of these is based on a ‘time of flight’ (ToF) mechanism which was considered subsequently by Ishikawa and Marshall [36] while analyzing their experimental data. Based on their physical interpretation of the experimental data, Ishikawa and Marshall concluded that their data do not support the ToF mechanism. In contrast, invoking some subtle features of TASEP, which represents IFT in our model, we argue that the experimental observations of Ishikawa and Marshall are consistent with the ToF mechanism.

Note that equation (15) can be expressed as

$$\frac{d\langle L(t) \rangle}{dt} = k_1 C_p T(\langle L \rangle) - k_2 \quad (43)$$

with $k_1 = J\Omega_e$, $C_p = \langle N(t) \rangle / N_{\max}$, $T(\langle L \rangle) = e^{-2k\langle L(t) \rangle/v}$ and $k_2 = (1 - \rho)^2 \Gamma_r$. The form (43) looks exactly like the equation (1) in the supplementary information of reference [91]. However, the crucial difference between (43) and equation (1) in the supplementary information of reference [91] is that $T(\langle L \rangle)$ in (43) is given by a mathematical expression that follows naturally from the ToF mechanism whereas it was treated as a phenomenological parameter in reference [91].

The length-dependent growth and length-independent decay of flagella is at the foundation of Marshall and Rosenbaum’s ‘balance-point’ model [10]. It has been used also in a stochastic model of flagellar length control developed by Bressloff [92]. In the original version of the balance-point model [10] it was implicitly assumed that each IFT particle carries flagellar structural proteins as cargo. One of the key explicit assumptions of that version of the balance-point model was that the number of IFT particles and their average speed remain constant in time. Therefore, in that case, the decrease of the flagellar assembly rate with its increasing length could arise only if the rate of the arrival of the IFT particles decreased with the increase of flagellar length. But, this scenario was in direct contradiction with the subsequent experimental observation of Dentler [93]. In the revised balance-point model [18] an attempt was made to reconcile the balance-point concept with the experimental observation of Dentler [93] in terms of the variation in the sizes of the IFT trains (see [94] for an extension of the Bressloff’s work to a stochastic version of the revised balance-point model).

The length-dependent effective *assembly* rate and a length-independent *disassembly* rate of each individual flagellum in our model (see figure 2(a)) is consistent with the general concept of ‘balance-point’ [10, 18, 71]. However, the length-dependence of the effective assembly rate arises in our model from the *differential loading* of the IFT particles with flagellar structural proteins. The concept of differential loading was proposed earlier qualitatively [37, 38]; it is now incorporated quantitatively in our theoretical model.

Marshall and coworkers [95] developed an alternative model where kinesin motor proteins, that diffuse on their way back to the base from tip, serve as ‘rulers’. In this model the steady state length of the flagellum is given by

$$L_{ss} = \left(\frac{2ND\delta L}{d} \right)^{1/2} \quad (44)$$

where N is the number of diffusing motors, D is their diffusion constant, δL is the increment of flagellar length when a motor reaches its tip, and d is the rate of shortening (decay) of flagellar length. In spite of the differences in the underlying length control mechanisms the expressions (19) and (44) for L_{ss} , shares one common feature. The steady-state length of the flagellum is determined by the balance of the competing length-dependent growth rate and length-independent decay rate.

The more recent model developed by Fai *et al* [40] is based on Hendel *et al*’s postulate [95] that the diffusing kinesins act as rulers for length control. Fai *et al* [40] use IFT particles and motors interchangeably throughout the paper without explicitly stating that they do not distinguish between the two. In contrast, the model developed by Hendel *et al* [95] does not specifically represent the IFT particles. In fact, Hendel *et al* [95] assumed that ‘each motor is associated with an IFT particle carrying a fixed quantity of material’. The slight difference in the expressions for L_{ss} derived by Hendel *et al* [95] and that of Fai *et al* [40] arises from difference in the scenarios considered by the two. The two assumptions made by Hendel *et al* [95] are: (i) ‘a constant source of free motor protein at the tip’ and, (ii) ‘motors that have reached the base immediately transport back to the tip’. Under these special conditions (i.e., ‘no tubulin depletion’ and ‘instantaneous ballistic motion’ [40]), as Fai *et al* point out [40], the more general form of the expression L_{ss} reduces to that of Hendel *et al* [95]. In this sense Fai *et al*’s result is slightly more improved compared to that of Hendel *et al* [95]. One key feature of Fai *et al*’s flagellar length control model is that the rate of shortening of a flagellum is also length dependent. This is in sharp contrast to all the other models of balance-point scenario where shortening rates are independent of the flagellar length.

As we have discussed above, a balance point in the context of flagellar length control can arise from length-dependent rates of growth or/and shrinkage of axonemal MTs. In other words, at least one of the two competing rates (assembly and disassembly rates) should be length dependent [72]. In this way a balance emerges between the assembly and disassembly and gives rise to a time-independent average length of the filament in the steady-state. Specifically, in our model the balance point results from a length-dependent growth and length-independent shrinkage of the axonemal MTs. However, the existence of a balance point is not a unique feature of MTs. This phenomenon occurs also in actin filaments where the rates of attachment and detachment of subunits at the barbed and pointed ends can exactly balance each other provided at least one of them is length-dependent [72, 73].

10. Summary and conclusions

In this paper we have developed a rather general theoretical model for eukaryotic flagellar length control. This model successfully integrates the following ingredients within a single theoretical framework: (i) a ToF mechanism for length sensing, (ii) a length-dependent differential loading of the IFT particles [37, 38], and (iii) representation of IFT as a totally asymmetric simple exclusion process (TASEP).

We have analysed the model at two different levels. The intrinsic fluctuations in the quantities of interest are obtained analytically from the master equations and the Fokker–Planck equations, and numerically from MC simulations. Most of these results are new predictions that, in principle, can be tested experimentally. The deterministic rate equations derived from the master equations account for the well known time-dependent, as well as the steady-state, properties of the system.

Next we list the main results of our analysis. (a) Quantification of the length-dependent growth rate, in terms of the length-dependent differential loading of the precursor proteins, and length-independent shrinkage rate gives rise a mechanism of attaining the steady-state length L_{ss} ; this scenario is consistent with the concept of balance-point introduced, and elaborated, earlier in the literature [10, 18, 71].

(b) Our results highlight the important role of the population kinetics of the structural precursor proteins in the common shared pool at the base of the flagella. In some physiologically relevant range of parameters, we demonstrate that during ciliogenesis the elongating flagellum can overshoot beyond its steady-state length L_{ss} before relaxing back to L_{ss} . Such overshooting, although not reported so far, is expected to be observed in the parameter range that we propose.

(c) In the context of the length coordination between the two flagella of biflagellates, it has been known for decades that, during regeneration of the amputated flagellum the unamputated flagellum exhibits a non-monotonic variation of its length: initially it shortens till its length becomes just equal to that of the regenerating flagellum and beyond this point both the flagella grow together maintaining approximately

equal length till attaining their pre-amputation steady-state lengths. Our model not only reproduces this non-trivial collective dynamics of the two flagella over a wide range of parameter values, but also reveals new qualitatively different behaviours in parameter regimes that, to our knowledge, have not been explored in laboratory experiments.

(d) We have carried out a numerical analysis of our model mimicking the conditions under which the *in vivo* experiments were carried out by Ishikawa and Marshall [36] to test the validity of the ToF mechanism. We have argued that the experimental observations are not only consistent with the ToF mechanism, but also provide experimental support for the TASEP-based description of the traffic of IFT particles. Moreover, a different numerical study of our model demonstrates that it can capture the experimentally observed [15, 77, 78] role of depolymerase cytoskeletal motors in the resorption of flagella.

(e) The stochastic version of our model has made new predictions on the nature of correlations between fluctuations of the lengths of the two flagella in steady-state as well as in states far from the steady-state.

Thus, in spite of the simplifying assumptions, as listed in section 4, the model is remarkably successful in accounting for all the known phenomena in the context of flagellar length control in biflagellated eukaryotes. Moreover, it also makes new predictions on the nature of length fluctuations and on the role of the pool of flagellar structural proteins that, in principle, can be tested experimentally. Furthermore, the stochastic formulations of the model have laid down the foundation on which more detailed structures of the theories can be constructed in future for quadriflagellate and octoflagellate eukaryotes.

Acknowledgments

We thank Gaia Pigino for useful discussions. SP and DC thank the MPI-PKS for hospitality in Dresden where a major part of this work was done. DC also acknowledges support by SERB (India) through a J C Bose National Fellowship. "Open Access" publication of this article has been made possible by generous support from the Max-Planck-Society (MPG).

Appendix A. Derivation of rate equations for a single flagellum from master equations

Now we will write the master equations governing the evolution of length and pool population in terms of A , B and C -defined in equations (21)–(23). The complete set of master equations governing the length of the flagellum:

For $j = 0$

$$\frac{dP_L(j, t)}{dt} = - \left[e^{-Cj} \sum_{n=0}^{N_{\max}} \frac{n}{N_{\max}} P_N(n, t) \right] AP_L(j, t) + BP_L(j+1, t). \quad (A1)$$

For $j = 1$ to $j = L_{\max} - 1$

$$\begin{aligned} \frac{dP_L(j, t)}{dt} = & \left[e^{-C(j-1)} \sum_{n=0}^{N_{\max}} \frac{n}{N_{\max}} P_N(n, t) \right] AP_L(j-1, t) - \left[e^{-Cj} \sum_{n=0}^{N_{\max}} \frac{n}{N_{\max}} P_N(n, t) \right] AP_L(j, t) \\ & + BP_L(j+1, t) - BP_L(j, t). \end{aligned} \quad (A2)$$

For $j = L_{\max}$

$$\frac{dP_L(j, t)}{dt} = \left[e^{-C(j-1)} \sum_{n=0}^{N_{\max}} \frac{n}{N_{\max}} P_N(n, t) \right] AP_L(j-1, t) - BP_L(j, t). \quad (A3)$$

The complete set of master equations governing the precursor population:

For $n = 0$

$$\begin{aligned} \frac{dP_N(n, t)}{dt} = & -\omega^+ \left(1 - \frac{n}{N_{\max}} \right) P_N(n, t) + \omega^-(n+1) P_N(n+1, t) \\ & + \left[\sum_{j=0}^{L_{\max}} A e^{-Cj} P_L(j, t) \right] \left[\frac{(n+1)}{N_{\max}} P_N(n+1, t) \right] - BP_N(n, t). \end{aligned} \quad (A4)$$

For $n = 1$ to $n = N_{\max} - 1$

$$\frac{dP_N(n, t)}{dt} = \omega^+ \left(1 - \frac{(n-1)}{N_{\max}} \right) P_N(n-1, t) - \omega^+ \left(1 - \frac{n}{N_{\max}} \right) P_N(n, t) + \omega^-(n+1) P_N(n+1, t) - \omega^-(n) P_N(n, t)$$

$$+ \left[\sum_{j=0}^{L_{\max}} A e^{-Cj} P_L(j, t) \right] \left[\frac{(n+1)}{N_{\max}} P_N(n+1, t) - \frac{(n)}{N_{\max}} P_N(n, t) \right] + B[P_N(n-1, t) - P_N(n, t)]. \quad (\text{A5})$$

For $n = N_{\max}$

$$\begin{aligned} \frac{dP_N(n, t)}{dt} &= \omega^+ \left(1 - \frac{(n-1)}{N_{\max}} \right) P_N(n-1, t) - \omega^-(n) P_N(n, t) \\ &\quad - \left[\sum_{j=0}^{L_{\max}} A e^{-Cj} P_L(j, t) \right] \left[\frac{n}{N_{\max}} P_N(n, t) \right] + B P_N(n-1, t). \end{aligned} \quad (\text{A6})$$

Some well known probability relations are the following

$$\begin{aligned} \sum_{j=0}^{\infty} \{P(j, t)\} &= 1 \\ \sum_{j=0}^{\infty} \{jP(j, t)\} &= \langle j(t) \rangle \\ \sum_{j=0}^{\infty} \{j^2 P(j, t)\} &= \langle j^2(t) \rangle. \end{aligned} \quad (\text{A7})$$

Multiplying both the sides of the master equation (A2) with j and summing it over, we get

$$\begin{aligned} \sum_{j=0}^{L_{\max}} j \frac{d}{dt} (P_L(j, t)) &= \sum_{j=0}^{L_{\max}} j \left[\underbrace{\left[\left\{ \sum_{n=0}^{N_{\max}} \frac{n}{N_{\max}} P_N(n, t) \right\} e^{-C(j-1)} A \right]}_{\text{term-1}} P_L(j-1, t) \right. \\ &\quad \left. - \underbrace{\left[\left\{ \sum_{n=0}^{N_{\max}} \frac{n}{N_{\max}} P_N(n, t) \right\} e^{-Cj} A \right]}_{\text{term-2}} P_L(j, t) + \underbrace{\{B\} P_{L1}(j+1, t) - \{(1-\rho)^2 \Omega_r\} P_{L1}(j, t)}_{\text{term-3}} \right] \end{aligned} \quad (\text{A8})$$

where L_{\max} is a positive integer and $L_{\max} \gg L_{ss}$.

On simplifying term-1 we will get

$$\begin{aligned} \text{Term - 1: } & \sum_{j=0}^{L_{\max}} j \left[\left\{ \sum_{n=0}^{N_{\max}} \frac{n}{N_{\max}} P_N(n, t) \right\} e^{-C(j-1)} A P_L(j-1, t) \right] \\ &= \left[\left\{ \sum_{n=0}^{N_{\max}} \frac{n}{N_{\max}} P_N(n, t) \right\} A \right] \left[\sum_{j=0}^{L_{\max}} \{j e^{-C(j-1)} P_L(j-1, t)\} \right] \\ &= \left[\left\{ \sum_{n=0}^{N_{\max}} \frac{n}{N_{\max}} P_N(n, t) \right\} A \right] \left[\sum_{j=0}^{L_{\max}} \{(j-1+1) e^{-C(j-1)} P_L(j-1, t)\} \right] \\ &= \left[\left\{ \sum_{n=0}^{N_{\max}} \frac{n}{N_{\max}} P_N(n, t) \right\} A \right] \left[\sum_{j=0}^{L_{\max}} \left\{ (j-1+1) \underbrace{e^{-C(j-1)} P_L(j-1, t)}_{\text{expand it}} \right\} \right] \\ &= \left[\left\{ \sum_{n=0}^{N_{\max}} \frac{n}{N_{\max}} P_N(n, t) \right\} A \right] \left[\sum_{j=0}^{L_{\max}} \{(j-1+1) (1 - C(j-1)) P_L(j-1, t)\} \right] \\ &= \left[\left\{ \sum_{n=0}^{N_{\max}} \frac{n}{N_{\max}} P_N(n, t) \right\} A \right] \left[\sum_{j=0}^{L_{\max}} \{(j-1) (1 - C(j-1)) P_L(j-1, t)\} \right] \\ &\quad + \sum_{j=0}^{L_{\max}} \{ (1 - C(j-1)) P_L(j-1, t) \} \end{aligned}$$

$$= \left[\left\{ \sum_{n=0}^{N_{\max}} \frac{n}{N_{\max}} P_N(n, t) \right\} A \right] \left[\{ (\langle L(t) \rangle - C \langle L(t)^2 \rangle) \} + \{ (1 - C \langle L(t) \rangle) \} \right]. \quad (\text{A9})$$

Similarly, on simplifying term-2 we will get

$$\text{Term - 2: } \sum_{j=0}^{L_{\max}} j \left[\left\{ \sum_{n=0}^{N_{\max}} \frac{n}{N_{\max}} P_N(n, t) \right\} e^{-Cj} A P_L(j, t) \right] = \left[\left\{ \sum_{n=0}^{N_{\max}} \frac{n}{N_{\max}} P_N(n, t) \right\} A \right] \left[\{ (\langle L(t) \rangle - C \langle L(t)^2 \rangle) \} \right]. \quad (\text{A10})$$

On simplifying term-3 we will get

$$\begin{aligned} \text{Term - 3: } \sum_{j=0}^{L_{\max}} j [\{B\} P_L(j+1, t) - \{B\} P_L(j, t)] &= \sum_{j=0}^{L_{\max}} [\{B\} (j+1-1) P_L(j+1, t) - \{B\} j P_L(j, t)] \\ &= [\{B\} (\langle L \rangle - 1) - \{B\} (\langle L \rangle)] = -B \end{aligned} \quad (\text{A11})$$

$$\begin{aligned} \frac{d\langle L_1(t) \rangle}{dt} &= \text{term 1 term 2 + term 3} \\ &= \underbrace{\left[\left\{ \sum_{n=0}^{N_{\max}} n P_N(n, t) \right\} A \right]}_{\text{term 1}} \underbrace{(1 - C \langle L \rangle)}_{\text{term 2}} - B \\ &= \frac{\langle N(t) \rangle}{N_{\max}} A e^{-C \langle L(t) \rangle} - B. \end{aligned} \quad (\text{A12})$$

Now let us consider the master equation for the precursor population at the pool given by equation (A5). Multiplying both the sides with n and summing it over, we get

$$\begin{aligned} \sum_{n=0}^{N_{\max}} n \frac{dP_N(n, t)}{dt} &= \sum_{n=0}^{N_{\max}} n \left[\underbrace{\omega^+ \left(1 - \frac{(n-1)}{N_{\max}} \right) P_N(n-1, t) - \omega^+ \left(1 - \frac{n}{N_{\max}} \right) P_N(n, t)}_{\text{term-1}} \right. \\ &\quad \left. + \underbrace{(n+1) P_N(n+1, t) \omega^- - n P_N(n, t) \omega^-}_{\text{term-2}} \right. \\ &\quad \left. + \underbrace{P_N(n+1, t) \left[\sum_{j=0}^{L_{\max}} \{ e^{-Cj} A P_L(m, t) \} \right] - P_N(n, t) \left[\sum_{j=0}^{L_{\max}} \{ e^{-Cj} A P_L(m, t) \} \right]}_{\text{term-3}} \right. \\ &\quad \left. + \underbrace{\{B\} P_N(n-1, t) - \{B\} P_N(j, t)}_{\text{term-4}} \right]. \end{aligned} \quad (\text{A13})$$

On simplifying term-1:

$$\begin{aligned} \sum_{n=0}^{N_{\max}} n \left[\omega^+ \left(1 - \frac{(n-1)}{N_{\max}} \right) P_N(n-1, t) - \omega^+ \left(1 - \frac{(n)}{N_{\max}} \right) P_N(n, t) \right] \\ = \sum_{n=0}^{N_{\max}} \left[(n-1+1) \omega^+ \left(1 - \frac{(n-1)}{N_{\max}} \right) P_N(n-1, t) - \omega^+ n \left(1 - \frac{(n)}{N_{\max}} \right) P_N(n, t) \right] \\ = \sum_{n=0}^{N_{\max}} \left[\left\{ (\langle N(t) \rangle + 1) - \frac{(\langle N^2(t) \rangle + \langle N(t) \rangle)}{N_{\max}} \right\} \omega^+ - \left\{ \langle N(t) \rangle - \frac{\langle N^2(t) \rangle}{N_{\max}} \right\} \omega^+ \right] \\ = \left[1 - \frac{\langle N(t) \rangle}{N_{\max}} \right] \omega^+. \end{aligned} \quad (\text{A14})$$

On simplifying term-2:

$$\sum_{n=0}^{N_{\max}} n [\omega^- (n+1) P_N(n+1, t) - \omega^- n P_N(n, t)] = \sum_{n=0}^{N_{\max}} [\omega^- (n+1-1) (n+1) P_N(n+1, t) - \omega^- n^2 P_N(n, t)]$$

$$\begin{aligned}
&= \omega^- \langle N^2(t) \rangle - \omega^- \langle N(t) \rangle - \omega^- \langle N^2(t) \rangle \\
&= -\omega^- \langle N(t) \rangle.
\end{aligned} \tag{A15}$$

On simplifying term-3:

$$\begin{aligned}
&\sum_{n=0}^{N_{\max}} n \left(\frac{(n+1)}{N_{\max}} P_N(n+1, t) \left[\sum_{j=0}^{L_{\max}} \{ e^{-Cj} AP_L(j, t) \} \right] - \frac{(n)}{N_{\max}} P_N(n, t) \left[\sum_{j=0}^{L_{\max}} \{ e^{-Cj} AP_L(j, t) \} \right] \right) \\
&= \frac{1}{N_{\max}} \left[\sum_{j=0}^{L_{\max}} \{ e^{-Cj} AP_L(j, t) \} \right] \left[\sum_{n=0}^{N_{\max}} n \{ (n+1)P_N(n+1, t) - nP_N(n, t) \} \right] \\
&= \frac{1}{N_{\max}} \left[\sum_{j=0}^{L_{\max}} \{ e^{-Cj} AP_L(j, t) \} \right] \left[\sum_{n=0}^{N_{\max}} \{ (n+1-1)(n+1)P_N(n+1, t) - n^2 P_N(n, t) \} \right] \\
&= \frac{1}{N_{\max}} \left[\sum_{j=0}^{L_{\max}} \{ e^{-Cj} AP_L(j, t) \} \right] [\langle N^2(t) \rangle - \langle N(t) \rangle - \langle N^2(t) \rangle] \\
&= -\frac{\langle N(t) \rangle}{N_{\max}} \underbrace{\left[\sum_{j=0}^{L_{\max}} \{ e^{-Cj} AP_L(j, t) \} \right]}_{= -\frac{\langle N(t) \rangle}{N_{\max}} e^{-C\langle L(t) \rangle} A} = -\frac{\langle N(t) \rangle}{N_{\max}} e^{-C\langle L(t) \rangle} A.
\end{aligned} \tag{A16}$$

On simplifying term-4:

$$\begin{aligned}
\sum_{n=0}^{N_{\max}} n [\{B\} P_N(n-1, t) - \{B\} P_N(n, t)] &= \{B\} \sum_{n=0}^{N_{\max}} [(n-1+1)P_N(n-1, t) - nP_N(n, t)] \\
&= \{B\} [\langle N(t) \rangle + 1 - \langle N(t) \rangle] = B.
\end{aligned} \tag{A17}$$

On collecting all the terms:

$$\begin{aligned}
\frac{d\langle N(t) \rangle}{dt} &= \left[1 - \frac{\langle N(t) \rangle}{N_{\max}} \right] \omega^+ - \langle N(t) \rangle \omega^- - \frac{\langle N(t) \rangle}{N_{\max}} e^{-C\langle L(t) \rangle} A + B \\
&= \left[1 - \frac{\langle N(t) \rangle}{N_{\max}} \right] \omega^+ - \langle N(t) \rangle \omega^- - \frac{d\langle L(t) \rangle}{dt}.
\end{aligned} \tag{A18}$$

Appendix B. Steady state length distribution from master equation

In steady state, the probabilities become time dependent. So setting $\frac{dP_L(j,t)}{dt} = 0$ for the master equations given in equation (9), we get system of $L_{\max} + 1$ linear equations

$$\mu_{1,0}^L P_L(1) - \lambda_{0,1}^L P_L(0) = 0 \tag{B1a}$$

$$\lambda_{j-1,j}^L P_L(j-1) + \mu_{j+1,j}^L P_L(j+1) - (\lambda_{j,j+1}^L + \mu_{j,j-1}^L) P_L(j) = 0 \quad \text{for } j = 1 \text{ to } L_{\max} - 1 \tag{B1b}$$

$$\lambda_{L_{\max}-1,L_{\max}}^L P_L(L_{\max}-1) - \mu_{L_{\max},L_{\max}-1}^L P_L(L_{\max}) = 0. \tag{B1c}$$

Solving these coupled equations given by equation (B1) recursively, we obtain all the probabilities $P(j)$ for $j > 0$ in terms of $P(0)$. For example, $P(1)$ and $P(2)$ in terms of $P(0)$ are expressed as

$$P_L(1) = \frac{\lambda_{0,1}^L}{\mu_{1,0}^L} P_L(0) \quad (\text{B2a})$$

$$P_L(2) = \frac{(\lambda_{1,2}^L + \mu_{1,0}^L)}{\mu_{2,1}^L} P_L(1) - \frac{\lambda_{0,1}^L}{\mu_{2,1}^L} P_L(0) = \frac{(\lambda_{1,2}^L + \mu_{1,0}^L)}{\mu_{2,1}^L} \frac{\lambda_{0,1}^L}{\mu_{1,0}^L} P_L(0) - \frac{\lambda_{0,1}^L}{\mu_{2,1}^L} P_L(0) = \frac{\lambda_{1,2}^L \lambda_{0,1}^L}{\mu_{2,1}^L \mu_{1,0}^L} P_L(0). \quad (\text{B2b})$$

It can be shown by method of induction that

$$P_L(j) = P_L(0) \prod_{j'=0}^j \frac{\lambda_{j-1,j}^L}{\mu_{jj-1}^L}. \quad (\text{B3})$$

Substituting the expressions of $P(j)$, which are written in terms of $P(0)$, into to the following normalization condition

$$\sum_{j=0}^{L_{\max}} P_L(j) = 1 \quad (\text{B4})$$

we solve for $P_L(0)$ which turns out to be a function of the intensities $\lambda_{j,j+1}^L$ and $\mu_{j,j+1}^L$ ($j = 0, 1, \dots, L_{\max}$) and is given by

$$P_L(0) = \left[\left(1 + \sum_{j=0}^{L_{\max}} \prod_{i=1}^j \frac{\lambda_{i-1,i}^L}{\mu_{i,i-1}^L} \right) \right]^{-1}. \quad (\text{B5})$$

Hence, substituting the expression of for $P_L(0)$ obtained in equation (B5) in the formula for $P_L(j)$ given by equation (B3), all the $P_L(j)$ can be expressed in terms of transition rates λ_s^L and μ_s^L .

Appendix C. Steady state length distribution from Fokker–Planck equation

Carrying out a standard Kramer–Moyal expansion of the master equation, we get the Fokker–Planck equation

$$\frac{\partial P(x, t)}{\partial t} = -\frac{\partial}{\partial x} [f(x)P(x, t)] + \frac{\Delta L}{2} \cdot \frac{\partial^2}{\partial x^2} [g(x)P(x, t)] \quad (\text{C1})$$

with

$$f(x) = \lambda(x) - \mu(x) \quad (\text{C2})$$

and

$$g(x) = \lambda(x) + \mu(x) \quad (\text{C3})$$

where

$$\begin{aligned} \lambda(x) &= \frac{\langle N(t) \rangle}{N_{\max}} e^{-2kx/v} J\Omega_e \\ \mu(x) &= (1 - \rho)^2 \Gamma_r. \end{aligned} \quad (\text{C4})$$

In terms of $A = J\Omega_e \langle N(t) \rangle / N_{\max}$, $B = (1 - \rho)^2 \Omega_r$, and $C = \frac{2k}{v} f(x)$ and $g(x)$ can be re-written as:

$$\begin{aligned} f(x) &= Ae^{-Cx} - B \\ g(x) &= Ae^{-Cx} + B. \end{aligned} \quad (\text{C5})$$

The steady state solution of the Fokker Planck equation $P_{ss}(x)$ is given by:

$$P_{ss}(x) = C_0 \frac{e^{-\Phi(x)}}{g(x)} \quad (\text{C6})$$

where

$$\Phi(x) = -\frac{2}{\Delta L} \int_0^x \frac{f(x')}{g(x')} dx' = \frac{2}{\Delta L} \left[\frac{2}{C} \log \left(\frac{A + B e^{Cx}}{A + B} \right) - x \right] \quad (\text{C7})$$

and the normalization constant C_0 is given by

$$\begin{aligned}
\mathcal{C}_0 &= \left[\int_0^{L_m} \frac{e^{-\Phi(x')}}{g(x')} dx' \right]^{-1} \\
&= \left[A(C + \frac{2}{\Delta L}) \right]^{-1} \left[e^{L_m(C+2/\Delta L)} \left(\frac{A+B e^{CL_m}}{A+B} \right)^{-4/(C\Delta L)} {}_2F_1(\sigma_a, \sigma_b; \sigma_c; \sigma_{d1}) - {}_2F_1(\sigma_a, \sigma_b; \sigma_c; \sigma_{d2}) \right]
\end{aligned} \tag{C8}$$

where ${}_2F_1(a, b; c; z)$ represents the Gauss hypergeometric function and $\sigma_a = 1$, $\sigma_b = \frac{C-2}{C}$; $\sigma_c = \frac{2}{C} + 2$; $\sigma_{d1} = -\frac{B}{A}$, $\sigma_{d2} = -\frac{B}{A} e^{CL_m}$.

Substituting the expressions (C8) and (C7) for \mathcal{C}_0 and $\Phi(x)$, respectively, into the expression (C6) for $P_{ss}(x)$, we get

$$\begin{aligned}
P_{ss}(x) &= \left[A(C + \frac{2}{\Delta L}) \right] \left[\frac{1}{A+B} e^{[x(C+2/\Delta L)]} \left(\frac{A+B e^{Cx}}{A+B} \right)^{-4/(C\Delta L)-1} \right] / \\
&\quad \left[e^{L_0(C+2/\Delta L)} \left(\frac{A+B e^{CL_m}}{A+B} \right)^{-4/(C\Delta L)} {}_2F_1(\sigma_a, \sigma_b; \sigma_c; \sigma_{d1}) - {}_2F_1(\sigma_a, \sigma_b; \sigma_c; \sigma_{d2}) \right].
\end{aligned} \tag{C9}$$

Hence,

$$\begin{aligned}
\langle x \rangle_{ss} &= \frac{1}{\mathcal{C}_0} \frac{\Delta L}{A(C\Delta L + 2)^2} \left[\Delta L \left(\frac{A+B}{A} \right)^{4/(C\Delta L)} {}_3F_2(\eta_a, \eta_a, \eta_b; \eta_c, \eta_c; \eta_{d1}) \right. \\
&\quad + e^{L_m(C+2/\Delta L)} (A+B)^{4/(C\Delta L)} (A+B e^{CL_m})^{-4/(C\Delta L)} \left(1 + \frac{B e^{CL_m}}{A} \right)^{4/(C\Delta L)} \\
&\quad \times \left. \left\{ L_m(2 + C\Delta L) {}_2F_1(\eta_a, \eta_b; \eta_c; \eta_d) - \Delta L {}_3F_2(\eta_a, \eta_a, \eta_b; \eta_c, \eta_c; \eta_{d2}) \right\} \right] \tag{C10}
\end{aligned}$$

and

$$\begin{aligned}
\langle x^2 \rangle_{ss} &= \left[\frac{1}{\mathcal{C}_0} \right] \frac{\Delta L}{A(C\Delta L + 2)^3} \left[-2\Delta L^2 \left(\frac{A+B}{A} \right)^{4/(C\Delta L)} {}_4F_3(\eta_a, \eta_a, \eta_a, \eta_b; \eta_c, \eta_c, \eta_c; \eta_{d1}) \right. \\
&\quad + e^{L_m(C+2/\Delta L)} (A+B)^{4/(C\Delta L)} (A+B e^{CL_m})^{-4/(C\Delta L)} \left(\frac{B e^{CL_m}}{A} + 1 \right)^{4/(C\Delta L)} \\
&\quad \times \left. \left\{ L_m^2(C\Delta L + 2) {}_2F_1(\eta_a, \eta_b; \eta_c; \eta_{d2}) - 2\Delta L L_m(C\Delta L + 2) {}_3F_2(\eta_a, \eta_a, \eta_b; \eta_c, \eta_c; \eta_{d2}) \right. \right. \\
&\quad \left. \left. + 2\Delta L^2 {}_4F_3(\eta_a, \eta_a, \eta_a, \eta_b; \eta_c, \eta_c, \eta_c; \eta_{d2}) \right\} \right] \tag{C11}
\end{aligned}$$

where $\eta_a = \frac{2}{C} + 1$, $\eta_b = \frac{4}{C} + 1$, $\eta_c = \frac{2}{C} + 2$, $\eta_{d1} = -\frac{B}{A}$ and $\eta_{d2} = -\frac{B}{A} e^{CL_m}$.

Appendix D. Timescales

In terms of A , B and C , the coupled differential equations become:

$$\begin{aligned}
\frac{d[L(t)]}{dt} &= \frac{N(t)}{N_{\max}} A e^{-CL(t)} - B \\
\frac{d[N(t)]}{dt} &= \omega^+ \left[1 - \frac{N(t)}{N_{\max}} \right] - \omega^- N(t) - \frac{d[L(t)]}{dt}
\end{aligned} \tag{D1}$$

where $A = J\Omega_e$, $B = (1 - \rho)^2 \Gamma_r$, and $C = 2k/v$.

First we need to calculate the fixed point for the system. The system has one fixed point (L^*, N^*) , given by

$$L^* = \frac{1}{C} \log \left[\frac{A}{B} \frac{\omega^+}{\omega^- + (\omega^+/N_{\max})} \right] \tag{D2}$$

and

$$N^* = \frac{\omega^+}{\omega^- + (\omega^+/N_{\max})}, \quad (\text{D3})$$

which is the steady state of the system. Let $\frac{d[L(t)]}{dt} = f_L(L, N)$ and $\frac{d[N(t)]}{dt} = f_N(L, N)$.

Introducing the matrix

$$\begin{pmatrix} \frac{\partial f_L}{\partial L} & \frac{\partial f_L}{\partial N} \\ \frac{\partial f_N}{\partial L} & \frac{\partial f_N}{\partial N} \end{pmatrix} = \begin{pmatrix} -AC e^{-CL}N & A e^{-CL} \\ AC e^{-CL}N & -A e^{-CL} - \omega^- - \frac{\omega^+}{N_{\max}} \end{pmatrix} \quad (\text{D4})$$

and evaluating its elements at (L^*, N^*) , we get

$$\begin{pmatrix} -CB & B \left(\frac{\omega^-}{\omega^+} + \frac{1}{N_{\max}} \right) \\ C B & -B \left(\frac{\omega^-}{\omega^+} + \frac{1}{N_{\max}} \right) - \omega^- - \frac{\omega^+}{N_{\max}} \end{pmatrix}. \quad (\text{D5})$$

The matrix (D5) has two eigenvalues (λ_+, λ_-) and two corresponding eigenvectors (V_+, V_-) ; the eigenvalues are

$$\begin{aligned} \lambda_{\pm} = & \frac{1}{2} \left[- \left\{ B \left(\frac{\omega^-}{\omega^+} + \frac{1}{N_{\max}} \right) + \omega^- + \frac{\omega^+}{N_{\max}} + BC \right\} \right. \\ & \left. \pm \sqrt{\left\{ B \left(\frac{\omega^-}{\omega^+} + \frac{1}{N_{\max}} \right) + \omega^- + \frac{\omega^+}{N_{\max}} + BC \right\}^2 - 4BC \left(\omega^- + \frac{\omega^+}{N_{\max}} \right)} \right] \end{aligned} \quad (\text{D6})$$

and the corresponding eigenvectors V_{\pm} are

$$\begin{pmatrix} \frac{1}{2BC} \left[B \left(\frac{\omega^-}{\omega^+} + \frac{1}{N_{\max}} \right) + \omega^- + \frac{\omega^+}{N_{\max}} - BC \pm \sqrt{\left\{ B \left(\frac{\omega^-}{\omega^+} + \frac{1}{N_{\max}} \right) + \omega^- + \frac{\omega^+}{N_{\max}} + BC \right\}^2 - 4BC \left(\omega^- + \frac{\omega^+}{N_{\max}} \right)} \right] \\ 1 \end{pmatrix}. \quad (\text{D7})$$

To simplify the expressions, that also helps in more transparent physical interpretations, we introduce the symbols

$$\begin{aligned} \zeta_1 &= -B \left(\frac{\omega^-}{\omega^+} + \frac{1}{N_{\max}} \right) - \omega^- - \frac{\omega^+}{N_{\max}} \\ \zeta_2 &= BC \\ \zeta_3 &= 4BC \left(\omega^- + \frac{\omega^+}{N_{\max}} \right). \end{aligned} \quad (\text{D8})$$

In terms of ζ_1, ζ_2 and ζ_3 , the eigenvalues and eigenvectors can be recast as

$$\lambda_{\pm} = \frac{1}{2} [-(\zeta_1 + \zeta_2) \pm \{(\zeta_1 + \zeta_2)^2 - \zeta_3\}] \quad (\text{D9})$$

and

$$V_{\pm} = \begin{pmatrix} \frac{1}{2\zeta_2} [(\zeta_1 - \zeta_2) \pm \{(\zeta_1 + \zeta_2)^2 - \zeta_3\}] \\ 1 \end{pmatrix}. \quad (\text{D10})$$

Note that the dependence of λ_{\pm} on the three parameters ω^+, ω^- and N_{\max} , which together characterize the population kinetics of the precursor pool, have been shown explicitly in (D6). The composite parameters A, B and C , as stated before, characterize the flagellar elongation, timer relaxation and flagellar shrinkage, respectively. The inverse of these two eigenvalues indicate the two timescales of relaxation of small excursions away from the steady-state. Since λ_- is the larger of the two eigenvalues, the associated timescales $\tau_{\pm} = 1/\lambda_{\pm}$ satisfy $\tau_+ > \tau_-$.

In figure D1(a), we plot the $\langle L(t) \rangle$ vs t for different pairs of Ω_e and Γ_r . Note that $\langle L_{ss} \rangle$ remain same for all the different sets of parameters because the ratio of Ω_e and Γ_r is kept same for all the cases. It can be checked from the expression of eigenvalues from equation (D6) that the the timescale mainly depend on ω^- and BC . In figure D1(a), we are vary B over three decades by changing Γ_r over three decades and we observe that the time in which the $\langle L(t) \rangle$ mature vary by three decades as well.

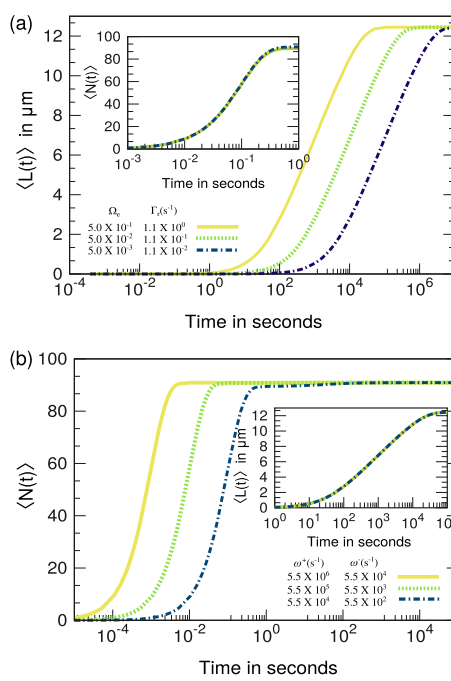


Figure D1. Timescales: (a) $\langle L(t) \rangle$ vs t . Inset: $\langle N(t) \rangle$ vs t . (b) $\langle N(t) \rangle$ vs t . Inset: $\langle L(t) \rangle$ vs t . Parameters: (a) $\rho = 0.1, J = 0.09, v = 0.9, k = 1.8 \times 10^{-3}, \omega^+ = 0.5, \omega^- = 5.0 \times 10^{-3}, N_{\max} = 1000, \delta t = 9.0 \times 10^{-6}$ s, $L(0) = N(0) = 0$ (b) $\rho = 0.1, J = 0.09, v = 0.9, k = 1.8 \times 10^{-3}, \Omega_c = 0.5, \Gamma_r = 1.0 \times 10^{-5}, N_{\max} = 1000, \delta t = 9.0 \times 10^{-6}$ s, $L(0) = N(0) = 0$.

Substituting the parameters used to plot figure D1(a) into the expressions (D6) for λ_{\pm} , we observe that λ_+ varies by three orders for the three different cases whereas λ_- remains practically unchanged. It indicates that λ_+ determines the timescale associated with the flagellar length $L(t)$. Moreover, from the inset of figure D1(a), we see that the timescale in which $N(t)$ attains $\langle N_{ss} \rangle$ is very small compared to the timescale in which $L(t)$ attain $\langle L_{ss} \rangle$. Besides, the curves for $\langle N_{ss} \rangle$ corresponding to the three sets of parameter values are almost identical. Hence, in this case, $\langle L(t) \rangle$ is given by the approximate expression (26) which clearly shows that, in this limit, the timescale in which $\langle L(t) \rangle$ attains $\langle L_{ss} \rangle$ is $\tau = 1/(BC)$. For consistency, we have also extracted the numerical value of λ_+ for all the three cases plotted in figure D1(a) and found it to be, indeed, approximately equal to $[BC]$. Hence, we conclude that $1/\lambda_+$ governs the timescale in which length $\langle L(t) \rangle$ attains $\langle L_{ss} \rangle$.

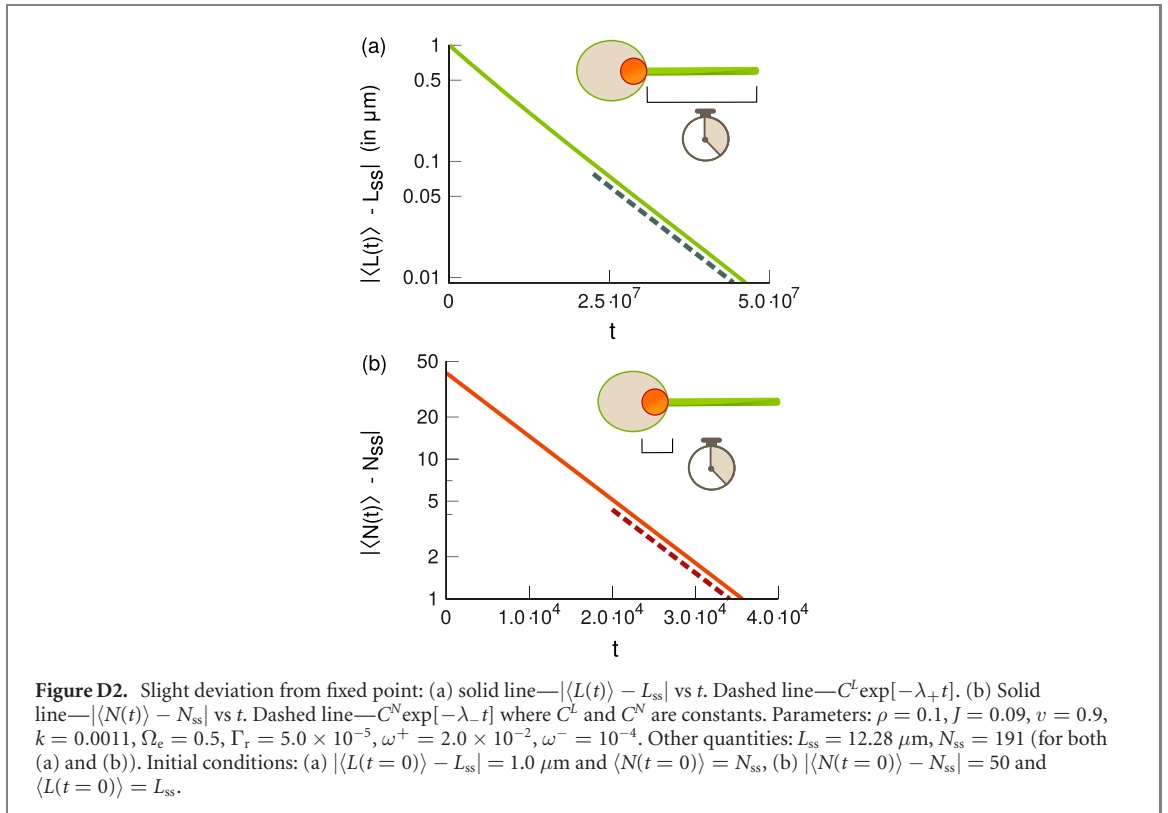
Similarly, to understand the timescale with which $\langle N(t) \rangle$ approach N_{ss} , we plot $\langle N(t) \rangle$ for different values of ω^+ and ω^- in figure D1(b). However, as the ratio of ω^+ and ω^- is kept same in all the three cases, N_{ss} is also same for all the cases. As we vary ω^- over three decades, the time over which $\langle N(t) \rangle$ attain steady state N_{ss} varies over three decades (figure D1(b)) while the corresponding $\langle L(t) \rangle$ attains steady state value $\langle L_{ss} \rangle$ in same time interval irrespective of the time taken by the pool to achieve steady value (see figure D1(b) inset).

To understand this observation, we computed the λ_{\pm} using the corresponding parameter values used to plot figure D1(b). We observed λ_- varies by three orders for the three different cases whereas λ_+ remains unchanged. For plotting figure D1(b), Γ_r is very small compared to ω^+ or ω^- (see the caption of figure D1). Therefore, under the approximation $B \simeq 0$, the formula for eigenvalues (16), can be approximated as

$$\lambda_- = \left[\omega^- + \frac{\omega^+}{N_{\max}} \right]. \quad (\text{D11})$$

Hence, we conclude that the timescale associated with the $N(t)$ dynamics is $\tau_- = 1/\lambda_- \approx 1/[\omega^- + (\omega^+/N_{\max})]$.

Finally, for further check of consistency, we perturbed the system slightly away from the fixed point (i.e., from the steady state) and observing how the perturbations died out with time. In the first case (see figure D2(a)), we have monitored the relaxation of the initial state $L(0) = \langle L_{ss} \rangle - \Delta L(0), N(0) = \langle N_{ss} \rangle$; the slope of the straight line on the semi-log plot is, indeed, λ_+ . Similarly, in the second case, we chose the initial condition $L(0) = \langle L_{ss} \rangle, N(0) = \langle N_{ss} \rangle - \Delta N(0)$; the slope of the straight line on the semi-log plot in figure D2(b) is also found to be λ_- .



Appendix E. Master equations for biflagellates

The master equations are given by

$$\frac{dP_{L_i}(j, t)}{dt} = \underbrace{\left[e^{-2k(j-1)/v} \sum_{n=0}^{N_{\max}} \frac{n}{N_{\max}} P_N(n, t) \right] J \Omega_e P_{L_i}(j-1, t) - \left[e^{-2kj/v} \sum_{n=0}^{N_{\max}} \frac{n}{N_{\max}} P_N(n, t) \right] J \Omega_e P_{L_i}(j, t)}_{\text{probabilistic assembly of the flagellar tip by the flux of full IFT particles}} + \underbrace{(1-\rho)^2 \Gamma_r P_{L_i}(j+1, t) - (1-\rho)^2 \Gamma_r P_{L_i}(j, t)}_{\text{stochastic disassembly of the tip when not occupied by any IFT particle}} \quad \text{where } i = 1, 2 \quad (\text{E1})$$

and the master equation governing the population of precursors in the pool is

$$\begin{aligned} \frac{dP_N(n, t)}{dt} = & \underbrace{\omega^+ \left(1 - \frac{(n-1)}{N_{\max}} \right) P_N(n-1, t) - \omega^+ \left(1 - \frac{n}{N_{\max}} \right) P_N(n, t)}_{\text{population dependent synthesis of flagella precursor by the cell.}} \\ & + \underbrace{[\omega^-(n+1) P_N(n+1, t) - \omega^-(n) P_N(n, t)]}_{\text{population dependent degradation of flagella precursor by the cell.}} \\ & + \underbrace{\left[\sum_{j=0}^{L_{\max}} J \Omega_e e^{-2kj/v} P_{L_1}(j, t) \right] \left[\frac{(n+1)}{N_{\max}} P_N(n+1, t) - \frac{(n)}{N_{\max}} P_N(n, t) \right]}_{\text{contribution of pool towards assembly of the first flagellum.}} \\ & + \underbrace{\left[\sum_{j=0}^{L_{\max}} J \Omega_e e^{-2kj/v} P_{L_2}(j, t) \right] \left[\frac{(n+1)}{N_{\max}} P_N(n+1, t) - \frac{(n)}{N_{\max}} P_N(n, t) \right]}_{\text{contribution of pool towards assembly of the second flagellum.}} \\ & + \underbrace{2(1-\rho)^2 \Gamma_r [P_N(n-1, t) - P_N(n, t)]}_{\text{addition of the precursor back to the pool when chipped from the tip of both the flagella during their disassembly.}} \quad (\text{E2}) \end{aligned}$$

Appendix F. Steps for simulating the model

We simulate our model using Monte Carlo methods. At a given instant of time t let the flagellar length be denoted by $L(t)$ and the pool population by $N(t)$. $L(t)$ can take discrete values $j = 0, \dots, L_{\max}$ and $N(t)$ can take discrete values $n = 0, \dots, N_{\max}$. We have chosen $L_{\max} \gg L_{\text{ss}}$.

At each Monte-Carlo time step, we update the values of $L(t)$ and $N(t)$ according to the following rules:

Updating the flagellar length: we generate a random number rn between 0 and 1. If at the current time step the flagellar length is $L(t) = j$, we update the length to $L(t) = j + 1$ if $\text{rn} < \lambda_{j,j+1}$ or update the length to $L(t) = j - 1$ if $\lambda_{j,j+1} < \text{rn} < \lambda_{j,j+1} + \mu_{j,j+1}$. While updating the length to $L(t) = j$ to $L(t) = j + 1$ we update the value of $N(t)$ from $N(t) = n$ to $N(t) = n - 1$. If there is no precursor in the pool ($N(t) = 0$), the length cannot be increased. Similarly, while updating the length to $L(t) = j$ to $L(t) = j - 1$ we update the value of $N(t)$ from $N(t) = n$ to $N(t) = n + 1$.

Updating the pool population: we generate a random number rn between 0 and 1. If at the current time step the pool population is $N(t) = n$, we update the pool population to $N(t) = n + 1$ if $\text{rn} < [\omega^+(1 - n/N_{\max})]$ or update the pool population to $N(t) = n - 1$ if $[\omega^+(1 - n/N_{\max})] < \text{rn} < [\omega^+(1 - n/N_{\max}) + \omega^- n]$.

ORCID iDs

Frank Jülicher  <https://orcid.org/0000-0003-4731-9185>

Debashish Chowdhury  <https://orcid.org/0000-0002-0536-2321>

References

- [1] Haldane J B S 1926 *On Being the Right Size* (New York: Harper's Magazine)
- [2] Marshall W F 2016 Cell geometry: how cells count and measure size *Annu. Rev. Biophys.* **45** 49–64
- [3] Marshall W F 2002 Size control in dynamic organelles *Trends Cell Biol.* **12** 414–9
- [4] Marshall W F 2015 Subcellular size *Cold Spring Harb. Perspect. Biol.* **7** a019059
- [5] Goehring N W and Hyman A A 2012 Organelle growth control through limiting pools of cytoplasmic components *Curr. Biol.* **22** R330–9
- [6] Ginger M L, Portman N and McKean P G 2008 Swimming with protists: perception, motility and flagellum assembly *Nat. Rev. Microbiol.* **6** 838–50
- [7] Cavalier-Smith T 1974 Basal body and flagellar development during the vegetative cell cycle and the sexual cycle of chlamydomonas reinhardtii *J. Cell Sci.* **16** 529–56
- [8] Cross F R and Umen J G 2015 The Chlamydomonas cell cycle *Plant J.* **82** 370–92
- [9] Quaranta L M and Parker J D K 2005 Cilia and the cell cycle? *J. Cell Biol.* **169** 707–10
- [10] Marshall W F and Rosenbaum J L 2001 Intraflagellar transport balances continuous turnover of the outer doublet microtubules: implications for flagellar length control *J. Cell Biol.* **155** 405–14
- [11] Mirvis M, Stearns T and Nelson W J 2018 Cilium structure, assembly, and disassembly regulated by the cytoskeleton *Biochem. J.* **475** 2329–53
- [12] Jeanneret R, Contino M and Polin M 2016 A brief introduction to the model microswimmer Chlamydomonas reinhardtii *Eur. Phys. J. Spec. Top.* **225** 2141
- [13] Wemmer K A and Marshall W F 2007 Flagellar length control in chlamydomonas- a paradigm for organelles size regulation *Int. Rev. Cytol.* **260** 175
- [14] Bloodgood R A 1974 Resorption of organelles containing microtubules *Cytobios* **9** 143–61
- [15] Liang Y, Meng D, Zhu B and Pan J 2016 Mechanism of ciliary disassembly *Cell. Mol. Life Sci.* **73** 1787–802
- [16] Quaranta L M 2004 Cellular deflagellation *Int. Rev. Cytol.* **233** 47–91
- [17] Johnson K A and Rosenbaum J L 1993 Flagellar regeneration in Chlamydomonas: a model system for studying organelle assembly *Trends Cell Biol.* **3** 156–61
- [18] Engel B D, Ludington W B and Marshall W F 2009 Intraflagellar transport particle size scales inversely with flagellar length: revisiting the balance-point length control model *J. Cell Biol.* **187** 81–9
- [19] Kozminski K G, Johnson K A, Forscher P and Rosenbaum J L 1993 A motility in the eukaryotic flagellum unrelated to flagellar beating *Proc. Natl Acad. Sci.* **90** 5519–23
- [20] Kozminski K G 2012 Intraflagellar transport- the ‘new motility’ 20 years later *Mol. Biol. Cell* **23** 751–3
- [21] Rosenbaum J L and Witman G B 2002 Intraflagellar transport *Nat. Rev. Mol. Cell Biol.* **3** 813
- [22] Lechtreck K F, Van De Weghe J C, Harris J A and Liu P 2017 Protein transport in growing and steady-state cilia *Traffic* **18** 277–86
- [23] Howard J 2001 *Mechanics of Motor Proteins and the Cytoskeleton* (Oxford: Oxford University Press)
- [24] Chowdhury D 2013 Stochastic mechano-chemical kinetics of molecular motors: a multidisciplinary enterprise from a physicist’s perspective *Phys. Rep.* **529** 1
- [25] Kolomeisky A B 2015 *Motor Proteins and Molecular Motors* (Boca Raton, FL: CRC Press)
- [26] Frey E, Parmeggiani A and Franosch T 2004 Collective phenomena in intracellular processes *Genome Inf.* **15** 46–55
- [27] Lipowsky R, Chai Y, Klumpp S, Liepelt S and Müller M J I 2006 Molecular motor traffic: from biological nanomachines to macroscopic transport *Physica A* **372** 34–51
- [28] Lipowsky R, Beeg J, Dimova R, Klumpp S and Müller M J I 2010 Collective behavior of molecular motors: cargo transport and traffic phenomena *Physica E* **42** 649–61
- [29] Leduc C, Campas O, Joanny J F, Prost J and Bassereau P 2010 Mechanism of membrane nanotube formation by molecular motors *Biochim. Biophys. Acta* **1798** 1418–26

[30] Appert-Roland C, Ebbinghaus M and Santen L 2015 Intracellular transport driven by cytoskeletal motors: general mechanisms and defects *Phys. Rep.* **593** 1–59

[31] Schadschneider A, Chowdhury D and Nishinari K 2010 *Stochastic Transport in Complex Systems: From Molecules to Vehicles* (Amsterdam: Elsevier)

[32] Derrida B 1998 An exactly soluble non-equilibrium system: the asymmetric simple exclusion process *Phys. Rep.* **301** 65–83

[33] Schütz G M 2001 *Phase Transitions and Critical Phenomena* ed C Domb and J L Lebowitz (New York: Academic)

[34] Mallick K 2015 The exclusion process: a paradigm for non-equilibrium behaviour *Physica A* **418** 17–48

[35] Ludington W B, Ishikawa H, Serebrenik Y V, Ritter A, Hernandez-Lopez R A, Gunzenhauser J, Kannegaard E and Marshall W F 2015 A systematic comparison of mathematical models for inherent measurement of ciliary length: how a cell can measure length and volume *Biophys. J.* **108** 1361–79

[36] Ishikawa H and Marshall W F 2017 Testing the time-of-flight model for flagellar length sensing *Mol. Biol. Cell* **28** 3447–56

[37] Wren K N, Craft J M, Tritschler D, Schauer A, Patel D K, Smith E F, Porter M E, Kner P and Lechtreck K F 2013 A differential cargo-loading model of ciliary length regulation by IFT *Curr. Biol.* **23** 2463–71

[38] Craft J M, Harris J A, Hyman S, Kner P and Lechtreck K F 2015 Tubulin transport by IFT is upregulated during ciliary growth by a cilium-autonomous mechanism *J. Cell Biol.* **208** 223–37

[39] Wemmer K, Ludington W and Marshall W F 2019 Testing the role of intraflagellar transport in flagellar length control using length altering mutants of Chlamydomonas *Phil. Trans. R. Soc.* **375** 20190159

[40] Fai T G, Mohapatra L, Kar P, Kondev J and Amir A 2019 Length regulation of multiple flagella that self-assemble from a shared pool of components *eLife* **8** e42599

[41] Lefebvre P A and Rosenbaum J L 1986 Regulation of the synthesis and assembly of ciliary and flagellar proteins during regeneration *Annu. Rev. Cell Biol.* **2** 517–46

[42] Fisch C and Dupuis-Williams P 2011 Ultrastructure of cilia and flagella- back to the future *Biol. Cell* **103** 249–70

[43] Lindemann C B and Lesich K A 2010 Flagellar and ciliary beating: the proven and the possible *J. Cell Sci.* **123** 519–28

[44] Sartori P, Geyer V F, Scholich A, Jülicher F and Howard J 2016 Dynamic curvature regulation accounts for the symmetric and asymmetric beats of Chlamydomonas flagella *eLife* **5** e13258

[45] Geyer V F, Sartori P, Friedrich B M, Jülicher F and Howard J 2016 Independent control of the static and dynamic components of the Chlamydomonas flagellar beat *Curr. Biol.* **26** 1098–103

[46] Wan K Y 2018 Coordination of eukaryotic cilia and flagella *Essays in Biochem.* **62** 829–38

[47] Taschner M and Lorentzen E 2016 The intraflagellar transport machinery *Cold Spring Harb. Perspect. Biol.* **8** a028092

[48] Lechtreck K F 2015 IFT-cargo interactions and protein transport in cilia *Trends Biochem. Sci.* **40** 765–78

[49] Prevo B, Scholey J M and Peterman E J G 2017 Intraflagellar transport: mechanisms of motor action, cooperation, and cargo delivery *FEBS J.* **284** 2905–31

[50] Pazour G J, Dixkert B L, Vusica Y, Seeley E S, Rosenbaum J L, Witman G B and Cole D G 2000 Chlamydomonas IFT88 and its mouse homologue, polycystic kidney disease gene Tg737, are required for assembly of cilia and flagella *J. Cell Biol.* **151** 709–18

[51] Buisson J, Chenouard N, Lagache T, Blisnick T, Olivo-Marin J and Bastin P 2013 Intraflagellar transport proteins cycle between the flagellum and its base *J. Cell Sci.* **126** 327–38

[52] Stepanek L and Pigino G 2016 Microtubule doublets are double-track railways for Intraflagellar transport trains *Science* **352** 721–4

[53] Taschner M, Bhogaraju S and Lorentzen E 2012 Architecture and function of IFT complex proteins in ciliogenesis *Differentiation* **83** S12

[54] Bhogaraju S, Engel B D and Lorentzen E 2013 Intraflagellar transport complex structure and cargo interactions *Cilia* **2** 10

[55] Cole D G and Snell W J 2009 SnapShot: intraflagellar transport *Cell* **137** 784

[56] Hao L and Scholey J M 2009 Intraflagellar transport at a glance *J. Cell Sci.* **122** 889–92

[57] Iomini C, Babaev-Khaimov V, Sassaroli M and Piperno G 2001 Protein particles in Chlamydomonas flagella undergo a transport cycle consisting of four phases *J. Cell Biol.* **153** 13–24

[58] Huet D, Blisnick T, Perrot S and Bastin P 2014 The GTPase IFT27 is involved in both anterograde and retrograde intraflagellar transport *eLife* **3** e02419

[59] Lefebvre P A 2009 Flagellar length control *The Chlamydomonas Source-Book: Cell Motility and Behavior* vol 3 ed G B Witmann (Amsterdam: Elsevier) pp 115–29

[60] Wingfield J L et al 2017 IFT trains in different stages of assembly queue at the ciliary base for consecutive release into the cilium *eLife* **6** e26609

[61] Cao M, Li G and Pan J 2009 Regulation of cilium assembly, disassembly and length by protein phosphorylation *Methods Cell Biol.* **94** 333–46

[62] Wang H, Gau B, Slade W O, Juergens M, Li P and Hicks L M 2014 The global phosphoproteome of Chlamydomonas reinhardtii reveals complex organelar phosphorylation in the flagella and thylakoid membrane *Mol. Cell. Proteomics* **13** 2337–53

[63] Pourquie O 2003 The segmentation clock: converting embryonic time into spatial pattern *Science* **301** 328–30

[64] Webb A B and Oates A C 2016 Timing by rhythms: daily clocks and developmental rulers *Dev. Growth Differ.* **58** 43–58

[65] Bhogaraju S, Taschner M, Morawetz M, Basquin C and Lorentzen E 2011 Crystal structure of the intraflagellar transport complex 25/27 *EMBO J.* **30** 1907

[66] Qin H, Wang Z, Diener D and Rosenbaum J 2007 Intraflagellar transport protein 27 is a small G protein involved in cell-cycle control *Curr. Biol.* **17** 193–202

[67] Bhogaraju S, Weber K, Engel B D, Lechtreck K F and Lorentzen E 2014 Getting tubulin to the tip of the cilium: one IFT train, many different tubulin cargo-binding sites? *Bioessays* **36** 463–7

[68] Fort C and Bastin P 2014 Boarder control on the IFT train *eLife* **3** e02531

[69] Wingfield J L and Lechtreck K F 2018 Chlamydomonas basal bodies as flagella organizing centers *Cells* **7** 79

[70] Wang Z, Fan Z C, Williamson S M and Qin H 2009 Intraflagellar transport (IFT) protein IFT25 is a phosphoprotein component of IFT complex B and physically interacts with IFT27 in Chlamydomonas *PLoS One* **4** e5384

[71] Marshall W F, Qin H, Brenni R and Rosenbaum J L 2005 Flagellar length control system: testing a simple model based on intraflagellar transport and turnover *Mol. Biol. Cell* **16** 270–8

[72] Mohapatra L, Goode B L, Jelenkovic P, Phillips R and Kondev J 2016 Design principles of length control of cytoskeletal structures *Annu. Rev. Biophys.* **45** 85–116

[73] Erlenkämper C and Kruse K 2009 Uncorrelated changes of subunit stability can generate length-dependent disassembly of treadmilling filaments *Phys. Biol.* **6** 046016

[74] Avasthi P and Marshall W F 2012 Stages of ciliogenesis and regulation of ciliary length *Differentiation* **83** S30–42

[75] Rosenbaum J L, Moulder J E and Ringo D L 1969 Flagellar elongation and shortening in Chlamydomonas *J. Cell Biol.* **41** 600–19

[76] Chien A, Shih S M, Bower R, Tritschler D, Porter M E and Yildiz A 2017 Dynamics of the IFT machinery at the ciliary tip *eLife* **6** e28606

[77] Piao T, Luo M, Wang L, Guo Y, Li D, Li P, Snell W J and Pan J 2009 Microtubule depolymerizing kinesin functions during both flagellar disassembly and flagellar assembly in Chlamydomonas *Proc. Natl Acad. Sci.* **106** 4713–8

[78] Wang L, Piao T, Cao M, Qin T, Huang L, Deng H, Mao T and Pan J 2013 Flagellar regeneration requires cytoplasmic microtubule depolymerization and kinesin-13 *J. Cell Sci.* **126** 1531–40

[79] Snell W J, Pan J and Wang Q 2004 Cilia and flagella revealed: from flagellar assembly in Chlamydomonas to human obesity disorders *Cell* **117** 693–7

[80] Hibbel A, Bogdanova A, Mahamdeh M, Jannasch A, Storch M, Schäffer E, Liakopoulos D and Howard J 2015 Kinesin Kip2 enhances microtubule growth in vitro through length-dependent feedback on polymerization and catastrophe *eLife* **4** e10542

[81] Rosenbaum J L and Child F M 1967 Flagellar regeneration in protozoan flagellates *J. Cell Biol.* **34** 345–64

[82] Howard J and Hyman A A 2007 Microtubule polymerases and depolymerases *Curr. Opin. Cell Biol.* **19** 31–5

[83] Varga V, Leduc C, Bormuth V, Diez S and Howard J 2009 Kinesin-8 motors act cooperatively to mediate length-dependent microtubule depolymerization *Cell* **138** 1174–83

[84] Walczak C E, Gayek S and Ohi R 2013 Microtubule-depolymerizing kinesins *Annu. Rev. Cell Dev. Biol.* **29** 417–41

[85] Lefebvre P A 1995 Flagellar amputation and regeneration in Chlamydomonas *Methods Cell Biol.* **47** 3–7

[86] Silva D A, Huang X, Behal R H, Cole D G and Qin H 2012 The RABL5 Homolog IFT22 regulates the cellular pool size and the amount of IFT particles partitioned to the flagellar compartment in Chlamydomonas reinhardtii *Cytoskeleton* **69** 33–48

[87] Chen Y T 1950 Investigations of the biology of Peranema trichophorum (Euglenineae) *J. Cell Sci.* **s3–91** 279–308

[88] Lewin R A 1953 Studies on the flagella of algae II: formation of flagella by chlamydomonas in light and darkness *Ann. New York Acad. Sci.* **56** 1091–3

[89] Coyne B and Rosenbaum J L 1970 Flagellar elongation and shortening in chlamydomonas *J. Cell Biol.* **47** 777–81

[90] Dentler W L and Rosenbaum J L 1977 Flagellar elongation and shortening in Chlamydomonas *J. Cell Biol.* **74** 747–59

[91] Ludington W B, Shi L Z, Zhu Q, Berns M W and Marshall W F 2012 Organelle size equalization by a constitutive process *Curr. Biol.* **22** 2173–9

[92] Bressloff P C 2006 Stochastic model of intraflagellar transport *Phys. Rev. E* **73** 061916

[93] Dentler W 2005 Intraflagellar transport (IFT) during assembly and disassembly of Chlamydomonas flagella *J. Cell Biol.* **170** 649–59

[94] Rathinam M and Sverchkov Y 2019 Stochastic dynamics of eukaryotic flagellar growth *Bull. Math. Biol.* **81** 2849–72

[95] Hendel N, Thomson M and Marshall W F 2018 Diffusion as a ruler: modeling kinesin diffusion as a length sensor for intraflagellar transport *Biophys. J.* **114** 663–74